

---

# Surface Catalysis and Characterization of Proposed Candidate TPS for Access-to- Space Vehicles

---

David A. Stewart, Ames Research Center, Moffett Field, California

July 1997



National Aeronautics and  
Space Administration

**Ames Research Center**  
Moffett Field, California 94035-1000



# Contents

	Page
Nomenclature .....	v
Summary .....	1
Introduction .....	1
Complex .....	1
Laser Facility .....	1
Side-Arm-Reactor Facility .....	2
Arc-Jet Facility .....	2
Tests Articles .....	2
Side-arm Reactor .....	2
Arc Jet .....	2
Candidate TPS .....	3
Experiment .....	4
Porosity Measurements .....	4
Side-Arm-Reactor Tests .....	4
Arc-Jet Tests .....	4
Analysis .....	5
Low-Temperature Coefficients (Side-Arm reactor) .....	5
High-Temperature Coefficients (Arc Jet) .....	5
SCFC Code .....	5
Test Results .....	9
Thermochemical Stability .....	9
Emittance .....	10
Surface Catalytic Efficiency .....	10
Surface Heating Distribution .....	11
Arc-Jet Case .....	11
Flight Case .....	12
Conclusions .....	12
Appendix A—Total Hemispherical Emittance .....	13
Appendix B—Surface Catalytic Coefficients .....	14
References .....	17
Tables .....	19
Figures .....	21



## Nomenclature

A	cross-section area, $\text{cm}^2$
C	relative atom concentration
$E_N$	nitrogen dissociation, $\text{MJ}/\text{cm}^3$
$H_T$	total enthalpy, $\text{MJ}/\text{kg}$
$h_D$	enthalpy of formation, $\text{MJ}/\text{kg}$
I	current, amps
k	constant
$k_w$	reaction rate constant, $\text{cm}/\text{s}$
$L_e$	Lewis number
M	molecular weight, $\text{gm}/\text{mole}$
m	mass loss rate, $\text{gm}/\text{s}$
$m_f$	mass flow rate, $\text{gm}/\text{s}$
P	pressure, atm
Pr	Prandtl number
$\dot{q}$	heat flux, $\text{W}/\text{cm}^2$
R	radius, cm
$\mathcal{R}$	gas constant, $\text{atm cm}^3/\text{gm mole K}$
$\mathcal{R}_{e2}$	Reynolds number
Sc	Schmidt number
s	arc length, cm
T	temperature, K
U	velocity, $\text{cm}/\text{s}$
V	voltage, volts
$\alpha$	mass fraction
$\gamma_a$	absolute recombination coefficient

$\gamma_i$	apparent recombination coefficient
$\epsilon$	emittance
$\mu$	viscosity, $\text{N}\cdot\text{s}/\text{m}^2$
$\rho$	density, $\text{gm}/\text{cm}^3$
$\sigma$	Stefan-Boltzmann constant

## Subscripts

A	air
abs	absolute
ch	chamber
e	boundary layer edge
eff	effective
F	flat-faced cylinder
f	frozen
H	hemisphere
i	chemical species
N	nitrogen
O	oxygen
o	stagnation point
th	total hemispherical
w	wall
$\infty$	free stream
2	behind bow shock wave

## Superscript

*	sonic point in nozzle throat
---	------------------------------



# Surface Catalysis and Characterization of Candidate TPS for Access-to-Space Vehicles

DAVID A. STEWART

*Ames Research Center*

## Summary

Surface properties have been obtained on several classes of thermal protection systems (TPS) using data from both side-arm-reactor and arc-jet facilities. Thermochemical stability, optical properties, and coefficients for atom recombination were determined for candidate TPS proposed for single-stage-to-orbit vehicles. The systems included rigid fibrous insulations, blankets, reinforced carbon carbon, and metals. Test techniques, theories used to define arc-jet and side-arm-reactor flow, and material surface properties are described. Total hemispherical emittance and atom recombination coefficients for each candidate TPS are summarized in the form of polynomial and Arrhenius expressions.

## Introduction

This report describes the research conducted as part of the Access-to-Space phase I study to develop a database on surface properties of candidate thermal protection systems (TPS) for a single-stage-to-orbit (SSTO) vehicle (ref. 1). Candidate systems include rigid fibrous insulations, flexible blankets, reinforced carbon carbon, and metallics.

During atmospheric entry, at hypersonic speed, the high temperature air between the bow shock wave and the TPS surface will be partially or fully dissociated into atoms. Therefore, the heat transferred to the surface of the TPS will consist of chemical as well as sensible energy. The chemical energy transferred (catalytic efficiency) to the surface of the TPS can strongly influence the heat transfer rate to the vehicle. For example, the Orbiter surface catalysis experiment demonstrated a 40% effect on the heat transfer rate during Earth entry (refs. 2–4). Therefore, to accurately size a TPS for any proposed SSTO vehicle, using one or a combination of materials, the designer must include the surface catalytic efficiency along with other surface properties such as thermochemical stability and emittance (refs. 5–9).

In this study, thermochemical stability, emittance, and atom recombination coefficients for 16 candidate SSTO TPS materials are reported. The Laser Accurate Surface-catalytic Efficiency Research (LASER) complex, test

techniques, and theories developed at Ames Research Center to obtain these surface properties and calculate atom recombination coefficients are reviewed (refs. 10–12).

The author gratefully acknowledges the support of Y. K. Chen in obtaining the BLIMPK code solutions, and of J. Marschall and J. Pallix in obtaining the coefficients from the side-arm reactor. These tasks were supported under Eloret Institute contract NCC2-462. Laser-induced fluorescence diagnostic measurements were conducted by Douglas Bamford under a NASA Small Business Research Program contract NAS2-13469.

## Complex

Ames Research Center has the unique capability of being able to obtain the surface properties, including catalytic efficiency, of candidate materials from a single laser complex located at Ames (fig. 1). The complex consists of a dye laser, a side-arm-reactor facility, and an arc-jet facility that are interactive. The central location of the laser provides for the use of laser-induced fluorescence (LIF) diagnostic techniques to determine the relative specie concentration levels in both the side-arm reactor (fig. 1(a)) and free-arc-jet streams (fig. 1(c)). The complex greatly reduces the cost and time required for obtaining surface properties of candidate TPS materials from room temperature to their upper use temperature.

## Laser Facility

The dye laser used to excite the atoms in the tube containing the sample is located in a room next to the side-arm-reactor facility (fig. 1(b)). A schematic of the laser system integrated with the side-arm-reactor components is shown in figure 2(a). The system was developed by Bamford and Romanovsky (ref. 13). A frequency-tripled Nd:YAG laser (Continuum NY81) pumps a tunable dye laser (Continuum ND60, Dual Grating Option) to excite oxygen or nitrogen atoms in either of the facilities. To detect oxygen atoms, Coumarin 460 laser dye is used to produce tunable radiation in the 452 nm region. For nitrogen, Stilbene 420 dye is used to

produce tunable radiation near 422 nm. The beam from the dye laser is passed through a doubling crystal of beta-barium borate (BBO) to produce the appropriate ultraviolet wavelength. The ultraviolet radiation is separated from residual blue radiation with a Pellin-Broca prism and is reflected off several dielectric mirrors and quartz prisms toward the arc-jet or side-arm-reactor test cell. The beam is used to excite the oxygen or nitrogen atoms in the test region via a two-photon transition at either 226 or 211 nm, respectively. Fluorescence by the atoms is detected using one or more gated photomultiplier tubes in conjunction with the appropriate narrow band filter for wavelengths at 845 nm (oxygen) and 869 nm (nitrogen). Signals are collected using gated integrators and are stored on a computer.

### **Side-Arm-Reactor Facility**

The side-arm-reactor facility (fig. 1(c)) essentially consists of a gas delivery and pressure control system coupled to a tubular reactor made up of a main arm and a dead-end side arm. High purity gases are fed into the reactor through a metering valve and the gas flow is measured using Tylan mass flow meters. The system is evacuated using turbo-molecular and roughing pumps. The system pressure is monitored using Baratron-type capacitance manometer gauges, and the target pressure is obtained by adjusting the gas inflow.

A microwave-discharge cavity located just upstream of the side-arm section was used to dissociate the test gas into atoms. A hinged heavy-duty electric furnace (68 cm long), positioned around the reactor section (side arm) of the facility, was used to raise the temperature of the test samples. The heater was located several centimeters away from the Tee junction formed by the main line and the side-arm section. The wall temperature within the side arm can be varied from 300 to 1300 K. A typical test specimen (1 to 27 cm long) is positioned at the center of the heater. Either a thermocouple probe (ref. 12) or LIF diagnostics can be used to obtain the data necessary for calculating the atom recombination coefficients (ref. 11).

Earlier coefficients were calculated using a thermocouple probe (consisting of a platinum/platinum/13% rhodium thermocouple and coated with either manganese or silver) to measure the temperature distribution along the center-line of the tube containing the test specimen. The reproducibility of the thermocouple measurements was within 1%. The present method uses LIF measurements to obtain the distribution of the specie concentration through this area of the tube. The atoms are excited by the laser energy focused through the end of the side arm, and the radiation from the excited atoms is measured using photomultiplier tubes which are aligned with the ports in the side wall of

the heater. The reduction in atom concentration along the tube is used to determine the atom recombination coefficient.

### **Arc-Jet Facility**

The typical measuring equipment used to obtain data from the aerothermodynamic heating facility (AHF) at Ames Research Center is shown in figure 2(b). The AHF uses a constricted arc heater to provide high-enthalpy dissociated hypersonic flow over a test model positioned downstream of a 16 deg conical nozzle. Either nitrogen or air can be easily used as the test gas without altering the heater hardware. This permits quick, consecutive measurements of heat flux and temperature to be taken from a test model during its exposure to either test gas. Surface conditions on the test model are varied by changing the exit diameter of the nozzle, the reservoir pressure, or the electrical power dissipated in the arc heater. The geometric area ratio (nozzle exit to throat) of the facility can be varied from 64 to 400. Heater pressure can be varied from 0.68 atm to roughly 5.5 atm and the maximum power dissipation in the heater can be increased up to 20 MW. Stagnation point enthalpy was determined using a nozzle code in conjunction with velocity measurements taken using a LIF diagnostic technique (ref. 10).

### **Test Articles**

Atom recombination coefficients were obtained by conducting tests on samples of the actual candidate TPS in both the arc-jet and side-arm-reactor facilities.

### **Side-Arm Reactor**

Split tube or short tubular sections of the proposed TPS were used in the side-arm reactor to obtain data needed to calculate the recombination coefficients (fig 1(c)). The thermal control coating was applied to the inside surface of split tubes made from materials such as rigid fibrous insulation or carbon. Fabric and metallic materials were tested as liners inside a quartz tube. Depending on the material's relative catalytic efficiency, tube lengths ranged from 2.5 cm to as much as 22.86 cm. The inside diameter of the tube was roughly 1.9 cm.

### **Arc Jet**

The arc-jet test configurations were designed to provide an adiabatic back wall and ensure uniform temperature and pressure distributions across the test samples. During the arc-jet tests, two different test configurations were

used to obtain data (fig. 3): a 5 deg flat-faced cone and a 15.2 cm diameter flat-faced cylinder. The flat-faced cone was made using rigid fibrous insulation (fig. 3(a)). It had an 8.3 cm base diameter, a 1.3 cm corner radius, and a thickness of 6.35 cm. A high emittance surface was developed by either coating or impregnation of the cone. A threaded aluminum mounting ring was bonded into the base of each cone so that it could be attached to a water-cooled support. Surface thermocouples (platinum/platinum 13% rhodium) were installed near the stagnation point of the cone.

The second configuration used samples cut in the shape of a 7.11 cm diameter disk. They were positioned at the center of the model by being mounted inside a retaining ring and backed by a disk of rigid fibrous insulation. The retaining ring, 7.62 cm in diameter and 6.25 cm thick, was also made from a coated rigid fibrous insulation. Finally, platinum/platinum/13% rhodium thermocouples were installed behind the sample, either in a plug (coated with a borosilicate glass) or in the surface of the backing material. This model holder resulted in the sample being recessed 0.3 cm below the front surface of the cylinder. Earlier arc-jet tests showed that the recessed mounting of the sample did not affect the surface temperature or heat flux relative to a flush-mounted sample (ref. 14).

## Candidate TPS

Candidate TPS materials used in this study are listed in table 1.

All candidate systems tested using the cone configuration (fig. 3(a)) were developed by Ames Research Center. These include:

1. Reaction-cured glass (RCG) (ref. 15) applied over a cone made using a mixture of silica and aluminoborosilicate fibers. RCG is basically a fully dense borosilicate glass roughly 0.030 cm thick.
2. Toughened unipiece fibrous insulation (TUFI), which consists mainly of a mixture of molybdenum disilicide and borosilicate glass (ref. 16). This system was impregnated into the surface of the insulation to a depth of 0.254 cm before being sintered in the furnace. The density of TUFI is roughly half of RCG. For this study, TUFI was impregnated into AETB-12, a mixture of aluminoborosilicate, silica, and alumina fibers.
3. Silicone-impregnated reusable ceramic ablator (SIRCA) made with a high purity silicon impregnated into a billet of FRCI-12 (a mixture of silica and aluminoborosilicate fibers) (ref. 17). Since SIRCA is an ablator (active system), its surface properties are

dependent on the aeroconvective heating environment used to form the char.

Flexible blanket systems (ref. 18) included in the study are:

1. Tailored advanced blanket insulation (TABI), developed by Ames Research Center, made using silicon carbide or aluminoborosilicate fibers (Nextel 440).
2. The Nextel 440 system coated with the protective ceramic coating (PCC), also developed by Ames Research Center. PCC basically consists of Ludox and uses silicon tetraboride (SiB<sub>6</sub>) as a flux and emittance agent.
3. The Nextel 440 system coated with the shuttle grey C-9 coating, developed by Rockwell International. The C-9 coating was made using tetraethyl orthosilicate (TEOS) glass along with a silicon carbide (SiC) emittance agent.

Coated advanced reinforced carbon carbon systems were provided by Langley Research Center, ROHR Incorporation, and McDonnell Douglas Aerospace (MDA). These coatings include:

1. C-CAT ACC-4, made by LTV and Carbon Advanced Technologies, which basically consists of a carbon composite with an SiC conversion coating treated with a TEOS glass and covered with a Type 1 sealant (sodium silicate-based glass).
2. LVP, a chemical vapor deposition (CVD) SiC/SiB glass containing zirconium oxide, which was made using a Loral and Vought Process.
3. ORCC (RT-42), obtained from ROHR, is a three-part system which consists of an initial sealer, an oxidation barrier (near stoichiometric mixture of B<sub>4</sub>C + SiC that was applied using CVD), and a borosilicate glass overglaze sprayed onto the samples.
4. Silicon carbide-silicon boride coated system, made by the Russians using CVD, was obtained from MDA. Finally, a sample of an uncoated SiC/SiC composite was provided by MDA for the study.

Surface sheets of the following candidate metallic TPS were characterized during this investigation:

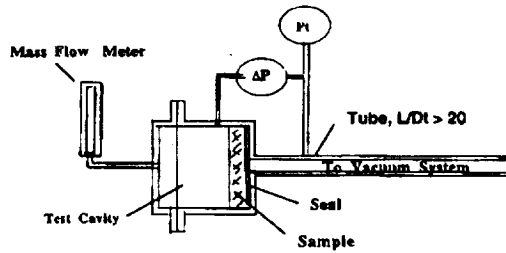
1. Oxidized and unoxidized samples of Inconel 617 (nickel-based material). The surface layer on the oxidized samples was the result of exposure for 2 hr in air at a temperature of 1256 K (1800°F) and a pressure of 1 atm. These samples were provided by MDA.

2. Oxidized samples of MA-956 (an iron-based material).
3. PM-1000, with a composition similar to Inconel 617, was provided by ROHR.

## Experiment

### Porosity Measurements

Open porosity of the surface on the rigid and flexible fibrous insulations is directly proportional to the material's effective surface area; therefore, it directly affects the surface catalytic efficiency. The open surface porosity of each material was determined using an apparatus illustrated in sketch 1.



Sketch 1

Using a very low mass-flow rate through the apparatus, the expression for conservation of mass, and Bernoulli's equation, the open-surface porosity of a TPS system can be calculated from the following equation:

$$A_{\text{eff}} = C \times m_f / D^2 (\Delta P \times P_1)^{1/2} \quad (1)$$

The calculated open-surface porosity for the silicon carbide cloth system was greater than 50%. The porosity of the other cloth systems and the TUF1 was below 10%. Porosity results in increased surface area, thereby increasing the surface catalytic efficiency above a value for a solid surface. The coefficients calculated from the data collected from both the arc jet and side-arm reactor are unique because they were obtained using the actual proposed TPS materials. Therefore, these apparent recombination coefficients include the effect of surface area (porosity) for each TPS. Earlier experiments carried out on a quartz surface in a side-arm reactor showed that the coefficient  $\gamma_i$  increased linearly with surface area (ref. 19):

$$\gamma_i = \gamma_{\text{abs}} S_a \quad (2)$$

Apparent coefficients establish the relative catalytic efficiency between materials and are required in order to

determine the total heat flux to the vehicle during high-speed Earth entry. The correction for surface area ( $S_a$ ) in equation (2) is equal to the ratio of the chemical active to the geometric surface areas. It should be made clear that many of the recombination coefficients reported in the literature and those presented here are not absolute values, but apparent values ( $\gamma_i$ ).

### Side-Arm-Reactor Tests

Tests in the side-arm reactor were conducted at constant pressure but at temperatures ranging between room temperature and 1250 K. The size of the power supply and microwave cavity was chosen in order to provide test conditions over a range of pressures from 0.1 to 1.0 torr. These experiments were conducted at 0.27 torr ( $3.5 \times 10^{-4}$  atm) using both high-purity molecular oxygen and nitrogen test gases. Data taken from this facility to determine the coefficients for the candidate systems were obtained over surface temperatures ranging from room temperature to 1250 K. Data collected from cloth systems in earlier studies were limited to much lower temperatures than the present study because of outgassing of the test specimen and the interaction of the volatiles with the thermocouple at this very low pressure (ref. 5).

To reduce the effect of outgassing on the data obtained from the cloth system, it was preconditioned in a vacuum furnace at 900 K and 2 mmHg for 24 hr to burn out the sizing material before exposure to the low-pressure side-arm-reactor environment. Using LIF diagnostic techniques and the preconditioned sample increased the temperature at which data could be taken from roughly 500 K to over 1200 K for the cloth systems.

### Arc-Jet Tests

Tests were also conducted using both nitrogen and air streams in the arc-jet facility. The models were exposed to the stream for 180 sec to ensure steady-state surface conditions during the measurements. Typical test conditions are shown in table 2. Arc-jet chamber pressure was varied from 0.68 to 4.1 atm and the power dissipation in the gas ranged from roughly 1.0 to 7.2 MW. Finally, a 60.96 cm diameter nozzle exit was used in this study (geometric area ratio between the nozzle exit and throat was 256). In addition, the mass flow through the heater was calculated using a fixed orifice size between the gas supply and the heater manifold. Total enthalpy (bulk) of the reservoir was then calculated using the following power and mass flow relationship:

$$H_T = \eta k IV / (m_f) \quad (3)$$

where

$\eta$  = efficiency factor (W. L. Love, private communication, 1987)

$k$  = conversion constant

Note that the bulk enthalpy was always lower than the effective enthalpy determined from the free-stream velocity measurements (table 2).

During each test the radiated energy from the stagnation region (roughly a 0.6 cm diameter area on the model) was measured using a radiometer with a bandwidth from 0.2 to 10.2  $\mu$ . Stagnation point pressure on the test models, located on the centerline and 35 cm downstream from the nozzle exit, was inferred from measurements taken with a water-cooled hemisphere. The surface pressure was measured using a bridge-type transducer with an accuracy of  $\pm 5\%$  full scale. In addition, pyrometer and thermocouple measurements were made to determine the surface temperature of each test sample. Samples were tested from one to five times over a range of surface temperatures from 1200 to 1730 K. Surface pressures ranged from 0.005 to 0.035 atm and effective enthalpies from 12.8 to 25 MJ/kg.

Pre- and posttest data were obtained from each sample in the form of photographs, reflectance measurements, and X-ray fluorescence analysis. These data included (1) room temperature spectral reflectance measurements using a BIO-RAD model FTS 40 (wavelength 0.25 to 2.5 microns) spectrophotometer and a Perkin Elmer model 310 (wavelength 2.5 to 20  $\mu$ ) spectrophotometer and (2) elemental chemical analysis of the surface of each sample using X-ray fluorescence measurements.

Finally, LIF diagnostic techniques (ref. 5) were used to aid in defining the free-stream properties in the hypersonic arc-jet streams.

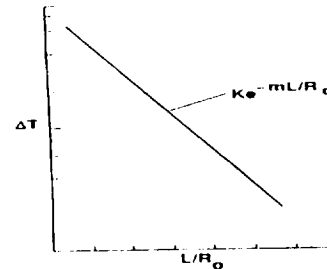
## Analysis

### Low-Temperature Coefficients (Side-Arm Reactor)

Low-temperature coefficients were obtained over a temperature range from room temperature to 1250 K using the side-arm reactor. In the past, coefficients were determined using data obtained from a thermocouple probe mounted along the centerline of the tube (refs. 17–19). The probe temperature increases because of atom recombination on its surface and is directly proportional to the local atom concentration. The temperature of the probe decreases as the probe is moved along the centerline of the tube, within the sample. For a first-order surface reaction, the temperature difference

between the probe and sample will decrease exponentially down the length of the tube (ref. 17).

A typical temperature distribution for the low catalytic efficiency material is illustrated in sketch 2.



Sketch 2

$$\Delta T = K \times \exp(-mL/R) \quad (4)$$

where

$$m = (V_m R k_A / 2 \cdot D_{12})^{1/2}$$

Equation (4) shows a relationship between the temperature difference ( $\Delta T$ ) and the distance along the tubular-shaped sample, derived by Smith (ref. 20) and Shuler and Laidler (ref. 21), to calculate the atom recombination coefficient. The constant ( $K$ ) in equation (4) depends on the heat transfer rate, gas transport properties, and probe surface catalytic efficiency. The recombination coefficient is directly related to the square of the slope of the  $\ln(\Delta T)$  versus  $L/R$  curve. Diffusion coefficients for atomic oxygen and nitrogen were empirically derived from the Chapman-Enskog equation using values of collision cross sections calculated by Yun and Mason (ref. 22). The thermal properties for these calculations were obtained from a thermal model derived by Cagliostro (private communication, 1994).

Currently, the atom recombination coefficients are calculated using measurements from LIF diagnostic techniques to obtain the specie concentration profile along the tube centerline. This technique was first demonstrated by Pallix and Copeland (ref. 23) for a relatively low catalytic efficiency material, a long tubular sample ( $L/D > 10$ ). Typical PMT signals and relative oxygen atom concentration profiles for both low and moderate catalytic efficiency materials are shown in figure 4. The signal profile for the low catalytic efficiency material (fig. 4(a)) is similar to the temperature profile shown in sketch 2. The coefficient can be calculated from the diffusion expression in equation (4) by substituting the slope of the PMT signal for  $\Delta T$ .

PMT signals representative of specie concentrations along the centerline of the tube for a moderately high catalytic efficiency material (silicon carbide/glass-coated cloth) are plotted relative to time and distance (fig. 4(b)). For this material the specie profile is no longer exponential along the centerline of the tube. Note that because of the high rate of atom recombination on its surface a much shorter sample was required. These data were obtained using a three-section diffusion tube (short sample of test material ( $L/D < 1$ ) positioned between two sections of quartz tube) which was placed at the center of the heater. Therefore, to calculate atom recombination coefficients for moderate and high catalytic efficiency materials, the basic diffusion equation must be solved using appropriate boundary conditions at the tube interfaces (ref. 12).

$$\frac{\partial^2 C}{\partial r^2} + \frac{1}{r} \frac{\partial C}{\partial r} + \frac{\partial^2 C}{\partial x^2} = 0 \quad (5)$$

where  $r$  and  $x$  are dimensionless cylindrical coordinates measured in units of tube radius and  $C = C(r,x)/C_0$  is the atom concentration normalized by the value at  $x = 0$ . This approach uses the same assumptions as the earlier method using the thermocouple: (1) gas phase recombination of atoms is negligible, (2) recombination of atoms on the wall of the sample is a first-order reaction, and (3) the side arm is at uniform temperature.

The LIF methods are more direct and less intrusive than using the thermocouple probe to obtain data for calculating the coefficients. A detailed description of the solutions for moderate and high efficiency materials is given in reference 12.

### High-Temperature Coefficients (Arc Jet)

Surface heat flux to the stagnation point of a test model exposed to arc-jet flow can be calculated using either a full Navier-Stokes code such as the General Aerodynamic Simulation Program (GASP) (ref. 24) or, if the flow is chemically frozen, a theory such as Goulard's (ref. 25). Computational differences in the two solutions are shown schematically in figure 5.

GASP was applied as an axisymmetric nonequilibrium air chemistry solution of the Navier-Stokes equations using a one-temperature model (fig. 5(a)). The two-factor approximate factorization algorithm and Van Leer flux vector splitting method (with upwind-biased third-order differencing) were incorporated into the solution using a global iteration scheme. A five-species (N, O, N<sub>2</sub>, O<sub>2</sub>, and NO) chemical reaction model was used in the code for air. The reaction rates applied in the solutions are from the work of Park (ref. 26).

In order to calculate the heat to the stagnation point on a test model, two GASP solutions are required: one for the nozzle flow and one for the flow through the bow shock wave and over the model. Therefore, axisymmetric grids are required to represent the flow through the nozzle and test section and the flow around the model. The code requires inputs of the heater conditions, atom recombination coefficients, and surface emittance for the materials during the arc-jet test to calculate the heat flux to the model. Also, the location of the model from the nozzle exit must be known. The formulation of this code is presented in detail in the GASP User's Manual (ref. 24).

Unlike GASP, Goulard's theory requires that the flow properties in the solution be obtained independently using a nozzle code. The general equation for Goulard's theory is:

$$\dot{q}_{w0} = 0.66 \text{Pr}^{-2/3} (\rho_2 \mu_2)^{1/2} \left[ \left( \frac{du_e}{ds} \right)_F \right]^{1/2} [H_{e0} - H_w] \times \left[ \frac{1 + (Le^{2/3} \phi_0 - 1) \alpha_0 h_D}{(H_0 - H_w)} + \frac{(Le^{2/3} \phi_N - 1) \alpha_N h_D}{(H_0 - H_w)} \right] \quad (6)$$

where

$$\phi_i = \left\{ \frac{1 + 0.47 S_c^{-2/3} \left[ 2 \left( \frac{du_e}{ds} \right)_F * \rho_2 \mu_2 \right]}{p_w k_{wi}} \right\}$$

Inputs required in Goulard's theory (based on a hemispherical-shaped configuration) are the gas properties from behind the bow shock wave and at the stagnation point of the model. These properties include the velocity gradient, wall reaction rate constant, and enthalpy. When the flow properties and velocity gradient are known, the reaction rate constants for a given material can be calculated from the equations by using a measured stagnation point heat flux and surface temperature as inputs.

### SCFC Code

In this study, a code was developed to calculate atom recombination coefficients and the total hemispherical emittance for advanced TPS using arc-jet data taken from test models in the shape of either a blunt cone (fig. 3(a)) or flat-faced cylinder (fig. 3(b)). Surface coefficients are calculated assuming frozen chemistry (SCFC) and incorporating Goulard's theory as part of a nozzle program written by Yoshishawa and Katzen (ref. 27). The program is based on the assumption that most properties of the gas in the test section (downstream of the nozzle), having

undergone relaxation of several internal degrees of freedom, are approximately the same as if the gas had made an instantaneous transition from full equilibrium flow to flow in which all internal energy exchange is frozen (fig. 5(b)). In one-dimensional flow, this process can be characterized by a parameter called the frozen Mach number ( $M_f$ ), which is used to define the state of the gas in the free stream.

In order to determine  $M_f$ , the effective area ratio of the test volume to nozzle orifice must first be estimated. Because impact pressure is relatively insensitive to  $M_f$ , it can be used along with the calculated bulk enthalpy (heater) to estimate the effective area ratio ( $A/A^*$ ). On the other hand, free-stream velocity, temperature, and atomic specie concentrations (oxygen and nitrogen mass fraction) in the flow are very sensitive to  $M_f$ . Figure 6 shows that the velocity increases by over 800 m/s and the nitrogen mass fraction (in both dissociated air and nitrogen streams) decreases by as much as 20% (0.2) between the total frozen chemistry condition ( $M_f = 1$ ) and equilibrium flow. In addition, for the same reservoir conditions, the amount of atomic nitrogen (mass fraction) present in a nitrogen stream is higher than for air.

**Free stream**— During this study, the flow properties (frozen Mach number) were obtained by iterating between the enthalpy and velocity, found from the LIF diagnostic techniques, until a minimum difference or agreement between measured and predicted velocity was reached (fig. 7). The resulting total enthalpy (effective enthalpy) was consistently 5% to 15% above the calculated bulk enthalpy values obtained using equation (3). However, the variations in enthalpy over the test conditions used for these tests were well within the performance envelope of the heater. The properties calculated using the LIF diagnostic technique will be referred to in this paper as “measured” values.

LIF-measured free-stream velocities were determined using the Doppler shifting of the fluorescence peaks of the nitrogen atoms and oxygen atoms in the nitrogen and air flows, respectively (fig. 7). Good agreement between measured and predicted values from the SCFC code was achieved for the velocity in most test cases for nitrogen. However, at the two lower test cases in air ( $P_{ch} = 0.68$  and 1.36 atm), the measured values could not be correlated any closer than about 5% to the predicted values (fig. 7). Further study is required in order to resolve the differences between the measured and predicted values because of uncertainty in the heater performance at low pressures. In addition, the frozen Mach numbers determined for the test cases were also substantiated by comparing measured and predicted values of nitrogen specie concentrations and translational temperatures in

air (figs. 8 and 9). Atomic nitrogen mass fraction in the hypersonic streams was plotted relative to the available amount of chemical energy per unit volume of gas available to dissociate molecular nitrogen during each test. The chemical energy per unit volume was calculated using the following expression:

$$E_N = \left\{ H_T - \left[ k / 2 (U_\infty)^2 + \alpha_N h_D \right] \right\} \rho_\infty \quad (7)$$

Atomic nitrogen concentrations in the free stream were plotted as normalized values relative to the amount of atomic nitrogen found to exist during test case 1 in air. Predicted values from the SCFC code account for the differences in the mass flow rates between test cases. In general, the predicted and measured values agreed well with each other for the air tests.

Also, measured values of translational temperature were calculated using the Gaussian line shapes (produced by a two-photon transition) that were recorded during the LIF experiments (fig. 9). Included in the figure are values assuming equilibrium flow and curves for  $M_f = 1.4$  and  $M_f = 2.5$  using the SCFC code. The SCFC calculation assumed that the translational, rotational, and vibrational temperatures were equal. The figures show clearly that the chemical state of the gas in the free stream during these tests correlates well with the predicted values near  $M_f = 2$ .

Within the accuracy of the LIF measurement technique, good agreement was found between all sets of calculated properties. The spread in the measured values was less for a series than for the overall test period.

**Effect of body geometry**— The bow shock wave strength and properties downstream are defined using the Knudsen number ( $Kn$ ).  $Kn = \lambda / \Delta$  is defined as the ratio of the mean free path of a gas ( $\lambda$ ) to the stand-off distance ( $\Delta$ ) relative to a hemisphere. For frozen flow, such as used in the SCFC code, the Knudsen number can be approximated from the free-stream Mach number and Reynolds number 2. One expression derived by Pai (ref. 28) which is applicable from continuum through the transitional flow regions is:

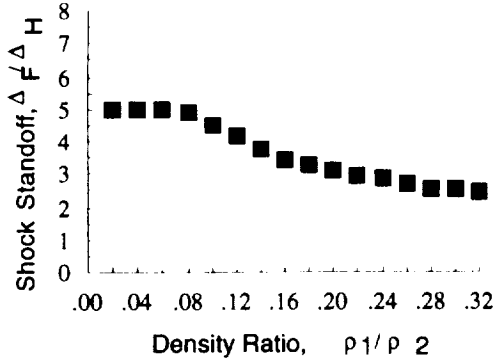
$$Kn = M_\infty / (\mathfrak{R}_2)^{1/2} \quad (8)$$

where

$$\mathfrak{R}_2 = (\rho_\infty U_\infty / \mu_2) D_H$$

The Knudsen number for a flat-faced configuration must be corrected to account for the difference in bow shock wave stand-off distance between it and a hemisphere.

The ratio of bow shock wave stand-off distances for a flat-faced configuration and hemisphere plotted as a function of the density ratio ( $\rho_2/\rho_1$ ) across the bow shock is illustrated in sketch 3.



Sketch 3

These values were calculated by Katzen and Kaattari, assuming equilibrium gas properties (ref. 29). The sketch shows that for weak bow shock waves ( $\rho_2/\rho_1 > 0.16$ ) the stand-off distance for a flat-faced configuration is roughly 2.5 times greater than for a hemisphere with the same base diameter. For strong bow shock waves ( $\rho_2/\rho_1 < 0.16$ ) the stand-off distance for the flat-faced configuration can increase to a value of greater than 5.0.

Based on the assumption of frozen chemistry, the Rankine-Hugoniot expression was used to calculate the density ratio across the bow shock wave in the SCFC code (ref. 26).

$$\rho_2 / \rho_\infty = (\gamma_f + 1) M_\infty^2 / (\gamma_f - 1) M_\infty^2 + 2 \quad (9)$$

where the free-stream specific heat ratio in the code was defined by the frozen state of the gas (ref. 30).

$$\gamma_f = c_p / c_v = \sum y_i c_{vi}$$

The density ratio calculated using equation (9) for the arc-jet test conditions (table 2) suggested that the bow shock wave was relatively weak with a density ratio near  $\rho_2/\rho_1 = 0.2$ . Therefore, the Knudsen number for the test models was reduced by a factor of 2.6 (sketch 3) from the calculated values for a hemisphere to account for the difference in their stand-off distances.

The Knudsen numbers calculated for the flat-faced test configurations (cylinder and cone) during the arc-jet tests are represented by the square and triangular symbols, respectively, in figure 10, which shows that the flow environment for the flat-faced cylinder was well within the viscous flow region and that the environment for the

blunt cone was within the merged layer flow region. Therefore, Goulard's theory provides an accurate flow simulation for the calculation of the heat transfer rate to the test configurations during these arc-jet tests.

Included in figure 10 is the typical operating envelope for both configurations in the AHF using nozzle exit diameters from 30.48 to 78.7 cm and enthalpies from 14.5 to 27.0 MJ/kg.

Differences in the velocity gradient at the stagnation point of the flat-faced test configurations and a hemisphere must also be accounted for in Goulard's theory (eq. (6)).

**Stagnation point heating**– In facilities with flows that are relatively frozen, the ratio of the velocity gradient at the stagnation point of a flat-faced cylinder and hemisphere has been shown to be directly proportional to the ratio of their heat fluxes (refs. 31 and 32):

$$\frac{(du_e / ds)_F}{(du_e / ds)_H} = (\dot{q}_F / \dot{q}_H)^2 \quad (10)$$

where, from Newtonian theory, the velocity gradient for a hemisphere is:

$$(du_e / ds)_H = 1 / R_H \sqrt{2 \cdot (p_w - p_\infty) / \rho_{e0}}$$

Over the operating envelope of the AHF, the relationship of the heat flux to a flat-faced cylinder and hemisphere with the same base radius was found to be linear (fig. 11). These data show that a linear relationship is valid for both cold-wall and hot-wall heat flux measurements. Therefore, the velocity gradient for the blunt cone was calculated by substituting the slope from this linear relationship into equation (6) and accounting for the exact location of the sonic point on the cylinder and blunt cone. However, the linear relationship in figure 11 would not necessarily be valid for all test facilities because of possible differences in the state of the gas in the free stream and shock layer.

Finally, calculating the atom recombination coefficients for both nitrogen and oxygen required the following basic assumptions: (1) a first-order reaction occurs on the surface of the material and (2) the accommodation coefficient for the material is equal to 1.0 and NO reactions are negligible.

With the first assumption, the following well known expression results:

$$\gamma_i = k_{wi} / \sqrt{(R T_w / 2 \cdot \pi M_i)} \quad (11)$$

**Relative coefficient for air**– The SCFC code also calculates a relative reaction rate constant ( $k_w$ ) for each

material using only air test data and the following semi-empirical relationship developed by Rosner (ref. 33):

$$k_w = (\rho_\infty U_\infty S_{th}) / \rho_w \cdot L_e^{2/3} \times [(\dot{q}_{wo} - \dot{q}_{min}) / (\dot{q}_{max} - \dot{q}_{wo})] \quad (12)$$

The parameters  $q_{min}$  and  $q_{max}$  were obtained from Goulard's theory by setting  $\phi = 0$  and  $\phi = 1.0$ , respectively. The parameter  $q_0$  is the same value used in equation (6) (measured radiated heat flux plus heat conduction into the model). The recombination coefficient ( $\gamma_A$ ) is calculated using equation (11).

**SCFC code validation**– In order to substantiate the predicted values for the free-stream and shock layer properties using the SCFC code, they were compared with predicted values using GASP.

Predicted properties for test cases 2, 3, and 4 are compared in figures 12–15. The GASP computation supports the frozen flow assumptions used in the SCFC code. Predicted free-stream specie concentrations, Mach number, and density ratio across the bow shock wave calculated from the SCFC code for the nitrogen test cases show good agreement with predicted values obtained using GASP.

For both air test cases the free-stream Mach numbers calculated using the SCFC code were within 10% of those calculated using GASP (figs. 13 and 15). The differences in Mach number are attributed to the slight variations in the calculated free-stream specific heat ratios (stream chemistry) between the two solutions. Therefore, the SCFC code coupled with LIF measurements can be used to reduce the cost, and the time required for determining atom recombination coefficients for candidate SSTO TPS is shortened from hours to minutes.

In addition to calculating the recombination coefficients, the code calculates the total hemispherical emittance ( $\epsilon_{th}$ ) using inputs of measured heat flux and surface temperature obtained during the arc-jet tests and the well known equilibrium reradiation equation:

$$\epsilon_{th} = \dot{q}_o / \sigma(T_w)^4 \quad (13)$$

Gas properties in the code are obtained from the Aerotherm Chemical Equilibrium (ACE) code (ref. 34) and using Gupta's thermodynamic properties (ref. 35).

## Test Results

### Thermochemical Stability

The effect of high-energy hypersonic flow on the stability of the candidate TPS was studied using X-ray fluores-

cence analyses, mass loss, and emittance measurements (figs 16–23). These data indicate that the rigid fibrous insulations and carbon composites coated with high viscosity glass systems remained relatively stable during arc-jet exposure. Carbon composites, with low viscosity glass coatings, and preoxidized metallics showed the loss of volatile species such as sodium, boron, and/or chrome and iron oxides after arc-jet exposure (figs. 16 and 17).

Removal of these elements is reflected in the mass loss data shown in figure 18. For example, the percent mass loss for the C-CAT composite sample increased with increased surface temperature (figs. 18(a) and 18(b)). The apparent weight gain of the LVP sample after an initial weight loss appears to be the result of the formation of ZrO during the arc-jet exposures (fig. 18(a)). Finally, the loss of chrome and iron oxides from the surface of the metallic samples had little effect on their mass loss histories (fig. 18(c)). The small mass loss experienced by these samples is believed to be the result of the initial oxides being converted into other forms by the presence of the atomic oxygen in the hypersonic air stream. Therefore, the metallic samples tested in this study must be classified as active TPS.

Another active TPS is SIRCA, a silicone-impregnated reusable ceramic ablator which dissipates the heat at high heat flux by mass removal. At low heat flux, where ablation does not occur, the heat is dissipated through equilibrium reradiation after the formation of a char. The char, predominantly a silicon-oxy-carbide ( $Si \cdot O_x \cdot C_y$ ), is created through endothermic chemical reactions during the arc-jet test. Therefore, its mechanical and surface thermal properties (emittance, catalytic efficiency, etc.) are not well defined, but depend directly on the specific aerothermodynamic heating environment to which they are exposed.

Thermochemical stability of SIRCA-15F in a convectively heated environment can best be illustrated by plotting the mass loss rate relative to surface temperature (fig. 18). The data used to develop the normalized mass loss rates plotted in this figure were obtained from reference 17. These earlier tests were also conducted in the AHF with similar stagnation point conditions (fully dissociated oxygen and partially dissociated nitrogen species). Figure 18 shows that SIRCA-15F starts to ablate at a surface temperature near 1800 K ( $q_{HW} = 52 \text{ W/cm}^2$ ). Included in the figure is a plot of the values for the  $B'_w$  function for SIRCA-15F. Arrhenius expressions for both the mass loss rate and  $B'_w$  function were obtained from curve fits to these data. These expressions, given below, can be used in heat shield design calculations.

Mass loss rate:

$$m/A = (1.0E-7)p^{0.8} e^{0.00811T_w} \quad (14)$$

$B'_w$  function:

$$B'_w = 1.6E-8 \epsilon^{0.00898T_w} \quad (15)$$

Figure 18(b) shows that the  $B'_w$  function for SIRCA-15F is independent of pressure; however, the range of pressures was limited during the tests (0.03 to 0.13 atm).

### Emittance

Thermochemical instability (loss of volatile species from the surface of the TPS) can affect not only the physical stability (mass loss, morphology, etc.) but the emittance of the TPS (figs. 20–23). These data show that arc-jet exposure of the samples using basically a glass matrix affected the spectral emittance throughout the short wavelength region (0.3 to 5.0  $\mu$ ) (fig. 20) and those using a basic silicon carbide matrix affected the spectra at the longer wavelengths (where the absorption band is located) (fig. 21). The absorption band for the coatings using a silicon carbide system occurred near 12 microns. For the nickel-based systems, the spectral hemispherical emittance increased over the entire wavelength range because of further oxidization of its surface during arc-jet exposure. For the iron-based system (MA-956), the emittance was not greatly affected by arc-jet exposure (fig. 23).

These changes in the spectral reflectance between pre- and posttest samples, due to the instability of the surface chemistry, have a direct effect on the total hemispherical emittance.

Calculated total hemispherical emittance from posttest samples using measured reflectance data is compared with values calculated using arc-jet data and the SCFC code (figs. 24–26). The values obtained from the reflectance data assume that the surface of the sample was opaque and they did not include the effect of temperature on the spectral hemispherical emittance. In general, the two sets of values agreed well for most samples with coatings using a basic glass matrix. The values calculated from arc-jet data for samples with SiC coating systems or oxidized metallic surfaces were lower than those obtained from the room temperature spectral reflectance data. In fact, for the SiC/SiC and ORCC systems the values obtained from the arc-jet data agreed better with the pretest calculated values. The spectral reflectance data (figs. 21(a) and 21(b)) show that an increased total hemispherical emittance should have resulted after arc-jet exposure because of the major effect it had on the absorption band for both samples. However, the

temperature effect on the reflectance data is unknown and could have a major effect on the result. One exception was the Russian SiC coating system. For this sample, both sets of emittance calculations were in good agreement with each other and, in fact, the trend in the values from the arc-jet data support the pre- and posttest results obtained from the reflectance data measured at room temperature. To fully understand the results of the total hemispherical emittance calculations for these TPS systems requires further study that includes the effects of temperature on the spectral reflectance data.

The total hemispherical emittance of both SIRCA and PM-1000 was dramatically changed by arc-jet exposure in air (figs. 24(c) and 26(c)). In both cases the endothermic reactions on the surface of these samples greatly affected the spectral hemispherical emittance, thereby resulting in large variations in their total hemispherical emittance. SIRCA, which initially has very low emittance at temperatures above 700 K, increased to values near 0.9; and PM-1000, which initially has very low values at temperatures below 1000 K, increased to values near 0.7 over the entire wavelength range after arc-jet exposure. However, for a flight case, the total hemispherical emittance of either TPS would not necessarily be the same values as obtained in the arc-jet test environment. Their emittance could be anywhere between the pre- and posttest extremes, depending on the flight trajectory and location on the vehicle.

Total hemispherical emittance for oxidized Inconel 617 and MA-956 showed little change after arc-jet exposure at temperatures above 1000 K. Values calculated using the arc-jet data were in close agreement with or slightly lower than those calculated from the reflectance data. Expressions were developed such that at the lower surface temperatures they predict values that are close to those calculated using room temperature reflectance data, and at the higher temperatures they are close to those calculated using arc-jet data. These expressions, illustrating the temperature dependence of each coated system, are summarized in Appendix A.

### Surface Catalytic Efficiency

Calculated coefficients for both nitrogen and oxygen atom recombination, obtained from data taken in the arc-jet and side-arm reactor, are plotted in figures 27–31. These values are represented by Arrhenius expressions,  $\gamma_i = ae^{(E/T_w)}$ , which are used in various reacting boundary layer or Navier-Stokes solutions to evaluate the effect of a material's catalytic efficiency on surface heating (refs. 24 and 36). The slope of the expression (E) is representative of the activation energy relative to surface reactions.

Expressions for RCG, PCC, C-9, TUF1, TAB1, and preoxidized Inconel 617 were derived from data taken in both arc-jet and side-arm-reactor facilities. Expressions for the remaining samples were calculated using data taken only from arc-jet tests. Coefficients for the candidate TPS can be grouped into three material classes: insulators (glass matrix), semiconductors, and metals (figs. 27–31).

For candidate TPS using a basic glass matrix, the variations in the coefficients with temperature are similar to RCG (fig. 27(a)). Because of viscosity, both nitrogen and oxygen coefficients for RCG increased and then decreased as the surface temperature approached its upper use limit. Similar trends were found in the coefficients for grey C-9, C-CAT, and the LVP systems (figs. 28(b), 29(c), and 29(d)). The characteristic reversal in the coefficients for these candidate glass systems occurred at temperatures much lower than for RCG. Insufficient data were collected on ORCC, precluding complete definition of the coefficients for the ORCC system. Coefficients for ORCC calculated using arc-jet data suggest that this unique characteristic occurs at a surface temperature below 1250 K (fig. 29(b)). Further study is required to fully define the Arrhenius expressions for ORCC over its entire range of use temperatures. PCC (a higher viscosity glass system than RCG) coated Nextel 440 was unique in that it exhibited the characteristic reversal in the coefficients for oxygen but not for nitrogen (fig. 28(c)).

SiC/SiC, TAB1, SIRCA char, Russian SiC, and TUF1 are grouped as semiconductor materials. Expressions for these systems have similar slopes for the oxygen and nitrogen coefficients. Note that the apparent activation energy (slope) for the oxygen atom recombination coefficients is positive and very high (>12,000) for all five samples. However, the activation energy for the nitrogen atom recombination coefficients for these systems is negative and varies over a wide range of values. The three systems with porosity (TUF1, SIRCA, and TAB1) had higher catalytic efficiency than those with nonporous surfaces (figs. 27(a), 27(c), and 28(a)). SIRCA had the highest value for the oxygen coefficient ( $\gamma_o = 0.46$  at 1367 K) and TUF1 the highest value for the nitrogen coefficient ( $\gamma_N = 0.33$  at 1811 K) of these systems. At this time it is not clear whether the increased catalytic efficiency of all three samples (TUF1, SIRCA, and TAB1) was only the result of surface porosity or was affected by surface chemistry.

Finally, the calculated values for Inconel 617 are plotted in figure 31. Arrhenius expressions used to fit both oxygen and nitrogen values have negative slopes and increase continuously with increasing temperature. Two Arrhenius expressions were required in order to define the

nitrogen coefficients, but only one to define the oxygen coefficients for this preoxidized metallic. Maximum values of the coefficient occurred at 1500 K ( $\gamma_N = 0.8$  and  $\gamma_o = 0.19$ ).

Arrhenius expressions for all candidate TPS, along with the temperature limits for their application, are summarized in Appendix B.

Coefficients derived from Rosner's expression (eq. (12)) are shown in figures 32 and 33. The air coefficients for the candidate TPS can also be divided into three groups in which their temperature dependences are:

1. Not influenced more by the recombination of either oxygen or nitrogen atoms. These TPS include coatings using basic glass matrices (RCG, C-CAT, C-9, and ORCC).
2. More strongly influenced by the recombination of nitrogen than of oxygen atoms (air coefficient increases with increased surface temperature). These TPS include basically systems that have high silicon carbide contained on their surface (TAB1, SiC/SiC, and SIRCA) and include Inconel 617.
3. More strongly influenced by the recombination of oxygen than of nitrogen atoms (air coefficient decreases with increased surface temperature). These TPS include TUF1, PCC, and the Russian SiC samples.

Arrhenius expressions for the air coefficients are included for each system in Appendix B. Unlike the individual coefficients for both nitrogen and oxygen atom recombination on an advance TPS, the air coefficients reflect their general catalytic efficiency. They are very useful in screening candidate TPS materials for application on advanced vehicles. However, the individual coefficients are required to properly size the TPS for a flight vehicle.

## Surface Heating Distribution

### Arc-Jet Case

To further validate the SCFC code for use in calculating atom recombination coefficients from arc-jet data, surface properties obtained from it for RCG (Appendices A and B) were used in GASP to calculate the surface temperature distributions over a 5 deg blunt cone for two arc-jet test cases (table 1, condition 2, for both nitrogen and air). The predicted values are compared with measured data taken during the tests (fig. 34). The predictions agree within 20 K of the measured data obtained from the model during the arc-jet tests in both

nitrogen and air. This is well within the accuracy of the temperature measurement.

### Flight Case

To illustrate the importance of the surface properties of individual candidate materials on the overall performance of the TPS during Earth entry on a spacecraft, the heating distribution along a generic SSTO vehicle's centerline was calculated. The SSTO configuration is simulated using a blunt-nosed 33 deg cone with nose radius of 1.55 m. The surface of the nose cap is covered with an RCG coating, and the fuselage with SiC TABI blankets.

The heating distribution was calculated using the reacting boundary layer code (BLIMPK) which was modified to include the wall energy balance for atom recombination and the surface emittance effect on the heating (ref. 36). These solutions were made for a trajectory point near where maximum heating would occur on the SSTO winged body at  $M_\infty = 22$  and at an altitude of 71.5 km (fig. 35).

First, the heating distribution along the centerline of the vehicle was calculated assuming equilibrium boundary layer flow. The small increase in temperature at the junction formed by the two materials is the result of the difference in their total hemispherical emittance. Second, a BLIMPK solution of the heating distribution along the centerline of the vehicle's midfuselage was calculated assuming that both the nose cap and fuselage were covered with a borosilicate glass. This solution showed that the surface temperatures were much lower than the solution assuming equilibrium boundary layer flow. Finally, a BLIMPK solution was obtained for the heating along the centerline of the vehicle assuming that an RCG glass nose cap and silicon carbide TABI covered the fuselage. This solution showed that the use of the two different materials would result in a large discontinuity in the temperature distribution at the junction where the glass-coated nose cap and blankets meet. At this junction, the surface temperature rapidly increased from a value for the RCG coated surface to a value above the one predicted assuming equilibrium boundary layer flow. Beyond the junction, the temperatures decrease toward values predicted assuming an equilibrium boundary layer over the surface of the vehicle. This large discontinuity in the heating distribution can have a major effect on the performance of the vehicle's TPS as well as its structure during an Earth entry and must be accounted for during the design.

### Conclusions

A facility (LASER complex) was described in which atom recombination coefficients for proposed TPS can be calculated over a wide range of temperatures. Theories for calculating the coefficients in both arc-jet and side-arm-reactor facilities were described.

1. LIF diagnostic techniques were required to accurately define the state of the gas during each test in the arc jet and specie concentrations in the side-arm reactor.
2. SCFC code, coupled with LIF measurements, provides a very fast, accurate method for determining the atom recombination coefficients for candidate TPS for future spacecraft.
3. Accurate predictions of the atom recombination coefficients of a candidate TPS require data from both side-arm-reactor and arc-jet facilities.
4. Predicted stagnation point surface temperature using atom recombination coefficients for RCG from the present SCFC code in GASP agreed well with measured values taken from the blunt cone during both nitrogen and air tests.

Surface properties of 16 candidate TPS were defined using data and theories developed during this study. These TPS include rigid fibrous insulations, reinforced carbon carbon, blankets, and metals.

1. Test data show that SIRCA and the metals must be classified as active TPS. Their thermochemical instability is reflected in optical properties and mass loss data obtained during the arc-jet tests.
2. In general, the total hemispherical emittance obtained from arc-jet data agreed well with values obtained from room temperature-measured reflectance data for TPS with a basic glass matrix, but overpredicted the values for those with SiC or oxidized surfaces.
3. Atom recombination coefficients for the candidate TPS can be summarized in three groups in which their temperature dependences are (1) not influenced more by either oxygen or nitrogen atom recombination (glass systems), (2) more strongly influenced by nitrogen atom recombination (SIRCA, SiC/SiC, and TABI), and (3) more strongly influenced by oxygen atom recombination (TUF1, PCC, and Russian SiC).

## Appendix A

### Total Hemispherical Emittance

#### Rigid Fibrous Insulations:

##### RCG

$$\epsilon_{th} = 0.89$$

##### TUF1

$$\epsilon_{th} = 0.89$$

##### \*\*\*\* SIRCA

$$\epsilon_{th} = 0.89 \text{ (arc-jet exposure)}$$

#### Blanket Systems:

##### TAB1

$$\epsilon_{th} = 0.836 + 8.27E-5Tw - 1.116E-7Tw^2$$

##### C-9 Coated Nextel 440

$$\epsilon_{th} = 0.873 - 1.26E-4Tw + 2.9E-7Tw^2 - 2E-10Tw^3$$

##### PCC Coated Nextel 440

$$\epsilon_{th} = 0.875 - 1.06E-4Tw + 1.78E-7Tw^2 - 1.89E-11Tw^3$$

#### Carbon Composite systems:

##### SiC/SiC

$$\epsilon_{th} = 0.667 + 2.28E-4Tw - 6.8E-8Tw^2$$

##### ORCC

$$\epsilon_{th} = 0.721 + 1.69E-4Tw - 5E-8Tw^2$$

##### C-CAT

$$\epsilon_{th} = 0.846 - 1.32E-5Tw$$

##### LVP

$$\epsilon_{th} = 0.896 - 1.2E-5Tw - 1.8E-8Tw^2$$

##### SiC Coated Russian ACC

$$\epsilon_{th} = 0.766 - 1.31E-4Tw - 3.2E-8Tw^2$$

#### Metals:

##### Oxidized Inconel 617

$$\epsilon_{th} = 0.626 - 7.7E-5Tw - 1.32E-8Tw^2$$

##### MA 956

$$\epsilon_{th} = 0.176 - 3.4E-4Tw - 7.2E-7Tw^2$$

##### PM-1000

$$\epsilon_{th} = 0.757 - 1.3E-4Tw - 1.0E-7Tw^2$$

## Appendix B

### Surface Catalytic Coefficients

Arrhenius expressions for the candidate TPS are listed below.

<b>Rigid Fibrous Insulations:</b>			
<b>RCG</b>			
<i>Nitrogen:</i>		(Tw < 764K)	
(Tw > 1575 K)	$\gamma_N = 6.2E - 6 \epsilon^{12100/Tw}$	(RN-1)	
(905K < Tw < 1575 K)	$\gamma_N = 10 \epsilon^{-10360/Tw}$	(RN-2)	
(465K < Tw < 905K)	$\gamma_N = 2.0E - 5 \epsilon^{1500/Tw}$	(RN-3)	
(Tw < 465K)	$\gamma_N = 5.0E - 4$	(RN-4)	
<i>Oxygen:</i>		(Tw < 764K)	$\gamma_N = 7E - 6 \epsilon^{1443/Tw}$ (TUN-2)
(Tw > 1617 K)	$\gamma_O = 39E - 9 \epsilon^{21410/Tw}$	(RO-1)	
(978 < Tw < 1617 K)	$\gamma_O = 5.2 \epsilon^{-8835/Tw}$	(RO-2)	
(502K < Tw < 978 K)	$\gamma_O = 1.6E - 4 \epsilon^{1326/Tw}$	(RO-3)	
(Tw < 502K)	$\gamma_O = 5.0E - 3 \epsilon^{-400/Tw}$	(RO-4)	
<i>Air:</i>		(Tw > 1324K)	$\gamma_O = 1.0E - 6 \epsilon^{14440/Tw}$ (TUO-1)
(Tw > 1653 K)	$\gamma_A = 1.5 \times 10^{-5} \epsilon^{12000/T}$	(RA-2)	
(1210 K < Tw < 1653 K)	$\gamma_A = 3.2 \epsilon^{-8285/Tw}$	(RA-1)	
		(685K < Tw < 1324K)	$\gamma_O = 10 \epsilon^{-6900/Tw}$ (TUO-2)
		(Tw < 685K)	$\gamma_O = 2.9E - 4 \epsilon^{264/Tw}$ (TUO-3)
		<i>Air:</i>	
		(1255K < Tw < 1644K)	$\gamma_A = 1.0E - 4 \epsilon^{9930/Tw}$ (TUA-1)
<b>TUFI</b>		<b>SIRCA</b>	
<i>Nitrogen:</i>		<i>Nitrogen:</i>	
(Tw > 764K)	$\gamma_N = 215 \epsilon^{-11730/Tw}$	(1255K < Tw < 1644K)	$\gamma_N = 1.27E - 3 \epsilon^{-16702/Tw}$ (SN- 1)
		<i>Oxygen:</i>	
		(1255K < Tw < 1644K)	$\gamma_O = 7.2E - 7 \epsilon^{18283/Tw}$ (SO-2)
		<i>Air:</i>	
		(1255K < Tw < 1644K)	$\gamma_A = 1.6 \epsilon^{-5250/Tw}$ (SA-3)
<b>TABI</b>		<b>Blankets Insulations:</b>	
<i>Nitrogen:</i>			
(Tw > 764K)	$\gamma_N = 215 \epsilon^{-11730/Tw}$	(Tw > 1302K)	$\gamma_N = 580 \epsilon^{-14149/Tw}$ (TAN-1)

(300K < Tw < 1302)	$\gamma_N = 0.025e^{-1006/Tw}$	(TAN-2)
<i>Oxygen:</i>		
(Tw < 1333K)	$\gamma_O = 1.0E^{-6e^{17080/Tw}}$	(TAO-1)
(470K < Tw < 1333K)	$\gamma_O = 5.0E^{-3490/Tw}$	(TAO-2)
(Tw < 470K)	$\gamma_O = 0.12e^{-1743/Tw}$	(TAO-3)
<i>Air:</i>		
(1255K < Tw < 1644K)	$\gamma_A = 0.45e^{-2582/Tw}$	(TAA- 1)

#### Grey C-9 Coated Nextel 440

<i>Nitrogen:</i>		
(Tw > 1321K)	$\gamma_N = 1.2E^{-7e^{17034/Tw}}$	(C9N-1)
(930K < Tw < 1321K)	$\gamma_N = 1.0e^{-4013Tw}$	(C9N-2)
(300K < Tw < 930K)	$\gamma_N = 0.02e^{-340/Tw}$	(C9N-3)
<i>Oxygen:</i>		
(Tw > 1312K)	$\gamma_O = 2.3E^{-3e^{4877/Tw}}$	(C9O-1)
(952K < Tw < 1312K)	$\gamma_O = 1.84e^{-3900/Tw}$	(C9O-2)
(300K < Tw < 952K)	$\gamma_O = 0.04e^{-253/Tw}$	(C9O-3)
<i>Air:</i>		
(1255K < Tw < 1644K)	$\gamma_A = 3.0E^{-6e^{13540/Tw}}$	(C9A-1)

#### PCC Coated Nextel 440

<i>Nitrogen:</i>		
(300K < Tw < 1644K)	$\gamma_N = 0.025e^{-460/Tw}$	(PCN- 1)
<i>Oxygen:</i>		
(Tw > 1316K)	$\gamma_O = 6.0E^{-6e^{13040/Tw}}$	(PCO-1)
(870K < Tw < 1316K)	$\gamma_O = 15e^{-6325/Tw}$	(PCO-2)
(Tw < 870K)	$\gamma_O = 0.02e^{-440/Tw}$	(PCO-3)
<i>Air:</i>		
(1255K < Tw < 1644K)	$\gamma_A = 2.0E^{-3e^{4024/Tw}}$	(PCA-1)

#### Carbon Composite Systems:

##### SiC/SiC

<i>Nitrogen:</i>		
(1255K < Tw < 1644K)	$\gamma_N = 10e^{-8888/Tw}$	(SC N-1)
<i>Oxygen:</i>		
(1255K < Tw < 1644K)	$\gamma_O = 4.0E^{-6e^{12348/Tw}}$	(SCO-1)
<i>Air:</i>		
(1255K < Tw < 1644K)	$\gamma_A = 0.26e^{-2895/Tw}$	(SCA-1)

#### ORCC Coated ACC

<i>Nitrogen:</i>		
(1255K < Tw < 1644K)	$\gamma_N = 1.0E^{-4e^{6623/Tw}}$	(ORN-1)
<i>Oxygen:</i>		
(1255K < Tw < 1644K)	$\gamma_O = 1.0e^{-7e^{15764/Tw}}$	(ORO-1)

*Air:*  
 (1255K < Tw < 1644K)  
 $\gamma_A = 1.0E^{-5} \epsilon^{10165/Tw}$  (ORA-1)

**C-CAT**

*Nitrogen:*  
 (Tw > 1475K)  
 $\gamma_N = 6.2E^{-6} \epsilon^{12100/Tw}$  (CTN-1)  
 (1255K < Tw < 1475K)  
 $\gamma_N = 4.0E^{-7} \epsilon^{7625/Tw}$  (CTN-2)  
*Oxygen:*  
 (Tw > 1359K)  
 $\gamma_O = 5.0E^{-8} \epsilon^{18023/Tw}$  (CTO-1)  
 (1255K < Tw < 1359K)  
 $\gamma_O = 13.5E^{-8} \epsilon^{8350/Tw}$  (CTO-2)  
*Air:*  
 (Tw > 1504K)  
 $\gamma_A = 2.0E^{-7} \epsilon^{17750/Tw}$  (CTA-1)  
 (1255K < Tw < 1504K)  
 $\gamma_A = 0.5E^{-4} \epsilon^{4410/Tw}$  (CTA-2)

**LVP Coated ACC**

*Nitrogen:*  
 (Tw > 1529K)  
 $\gamma_N = 1.5E^{-5} \epsilon^{10080/Tw}$  (LPN-1)  
 (1255K < Tw < 1529K)  
 $\gamma_N = 0.06E^{-2} \epsilon^{2605/Tw}$  (LPN-2)  
*Oxygen:*  
 (Tw > 1499K)  
 $\gamma_O = 2.5E^{-7} \epsilon^{17533/Tw}$  (LPO-1)  
 (1255K < Tw < 1499K)  
 $\gamma_O = 7.5E^{-8} \epsilon^{8283/Tw}$  (LPO-2)

*Air:*  
 (Tw > 1567K)  
 $\gamma_A = 3.0E^{-3} \epsilon^{2653/Tw}$  (LPA-1)  
 (1255K < Tw < 1567K)  
 $\gamma_A = 0.08E^{-2} \epsilon^{2518/Tw}$  (LPA-2)

**SiC Coated Carbon (Russian)**

*Nitrogen:*  
 (1255K < Tw < 1644K)  
 $\gamma_N = 0.074E^{-6} \epsilon^{2361/Tw}$  (RUN-1)  
*Oxygen:*  
 (1255K < Tw < 1644K)  
 $\gamma_O = 4.2E^{-8} \epsilon^{17533/Tw}$  (RUO-1)  
*Air:*  
 (1255K < Tw < 1644K)  
 $\gamma_A = 8.0E^{-4} \epsilon^{5040/Tw}$  (RUA-1)

**Metal Systems:**

**Inconel 617 (Preoxidized)**

*Nitrogen:*  
 (Tw > 758K)  
 $\gamma_N = 22.0E^{-4} \epsilon^{970/Tw}$  (ICN-1)  
 (300K < Tw < 758K)  
 $\gamma_N = 0.11E^{-9} \epsilon^{953/Tw}$  (ICN-2)  
*Oxygen:*  
 (300K < Tw < 1644K)  
 $\gamma_O = 0.55E^{-1} \epsilon^{1610/Tw}$  (ICO-1)  
*Air:*  
 (1255K < Tw < 1478K)  
 $\gamma_A = 1.7E^{-4} \epsilon^{15275/Tw}$  (ICA-1)

## References

1. Office of Space Systems Development, NASA Headquarters: Access to Space Study. Summary Report, Jan. 1994.
2. Stewart, D. A.; Rakich, J. V.; and Lanfranco, M. J.: Catalytic Surface Effect Experiment on Space Shuttle. *Thermophysics of Atmospheric Entry, Progress in Astronautics and Aeronautics*, vol. 82, T. E. Horton, ed., AIAA, New York, 1982, pp. 248–272.
3. Stewart, D. A.; Rakich, J. V.; and Lanfranco, M. J.: Catalytic Surface Effect Space Shuttle Thermal Protection System During Earth Entry of Flights STS-2 through STS-5. *Shuttle Performance: Lessons Learned*, NASA CP-2283, part 2, 1983.
4. Stewart, D. A.; Rakich, J. V.; and Chen, Y. K.: Flight Experiment Demonstrating the Effect of Surface Catalysis on the Heating Distribution over the Space Shuttle Heat Shield. *Orbiter Experiments (OEX) Aerothermodynamic Symposium*, Williamsburg, Va., Apr. 1993.
5. Stewart, D. A.; Pallix, J.; and Esfahani, L.: Surface Catalytic Efficiency of Candidate Ceramic Thermal Protection Materials for a SSTO. *CDTM-20007*, Mar. 1995.
6. Stewart, D. A.: Surface Catalytic Efficiency of Advanced Carbon Carbon Candidate Thermal Protection Materials for SSTO Vehicles. *TM X-110383*, Feb. 1996.
7. Henline, W. D.; Palmer, G. E.; Milos, F. S.; and Olynick, D. R.: Aerothermodynamic Heating Analysis and Heatshield Design of an SSTO Rocket Vehicle for Access-to-Space. *AIAA Paper 95-2079*, June 1995.
8. Tam, C. T.; and Olynick, D. R.: An Investigation of Possible Shuttle Upgrades Using Advanced TPS Concepts. *AIAA Paper 97-0277*, Jan. 1997.
9. Olynick, D. R.: Trajectory Based TPS Sizing for an X-33 Winged Vehicle Concept. *AIAA Paper 97-0276*, Jan. 1997.
10. Stewart, D. A.; Chen, Y. K.; Bamford, D. J.; and Romanovsky, A. B.: Predicting Material Surface Catalytic Efficiency using Arc-Jet Tests. *AIAA Paper 95-2013*, June 1995.
11. Stewart, D. A.: Determination of Surface Catalytic Efficiency for Thermal Protection Materials—Room Temperature to their Upper Use Limit. *AIAA Paper 96-1863*, June 1996.
12. Marschall, J.: Experimental Determination of Oxygen and Nitrogen Recombination Coefficients at Elevated Temperatures Using Laser-Induced Fluorescence. Submitted to the National Heat Transfer Conference, Baltimore, Md., Aug. 1997, *AIAA Paper 97-3879*.
13. Bamford, D. J.; and Romanovsky, D. J.: High Speed Velocity Diagnostics for NASA Ames Arc-Jet Facility. Phase II Final Report, Contract NAS2-13879, Dec. 1995.
14. Stewart, D. A.: Temperature Control Coatings. Tenth National Aero-Space Plane Technology Symposium, Vol. IV, Materials, NASP CP-10061, 1991, pp. 525–542.
15. Goldstein, H. E.; Leiser, D. B.; et al.: Reaction Cured Borosilicate Glass Coating for Low-Density Fibrous Silica Insulation. Plenum Corp., New York, *Borate Glasses*, 1978, p. 623.
16. Leiser, D. B.; Churchward, R.; Kavala, V.; Stewart, D. A.; and Balter, A.: Advanced Porous Coating for Low-Density Ceramic Insulation Materials. *J. Amer. Ceramic Soc.*, vol. 72, no. 6, 1989, pp. 1003–1010.
17. Tran, H.; Johnson, C.; Rasky, D.; and Hui, F.: Silicone Impregnated Reusable Ceramic Ablators for Mars Follow-on Missions. *AIAA Paper 96-1819*, June 1996.
18. Kourtides, D. A.; Chiu, S. A.; Iverson, D. J.; and Lowe, D. M.: Thermal Response of Rigid and Flexible Insulations and Reflective Coating in an Aeroconvective Heating Environment. *NASA TM-103925*, Mar. 1992.
19. Kim, Y. C.; and Boudart, M.: Recombination of O, N, and H Atoms on Silica: Kinetics and Mechanism. *Langmuir*, vol. 7, 1991, pp. 2999–3005.
20. Smith, W. V.: The Surface Recombination of H Atoms and OH Radicals. *J. Chem. Physics*, vol. 11, Mar. 1943, pp. 110–112.
21. Shuler, K. E.; and Laider, K. J.: The Kinetics of Heterogeneous Atom and Radical Reactions. *J. Chem. Physics*, vol. 17, 1949, p. 1212.
22. Yun, K. S.; and Mason, E. A.: Collision Integrals for the Transport Properties of Dissociating Air at High Temperatures. *Phys. Fluids*, vol. 5, no. 4, 1961, pp. 380–386.

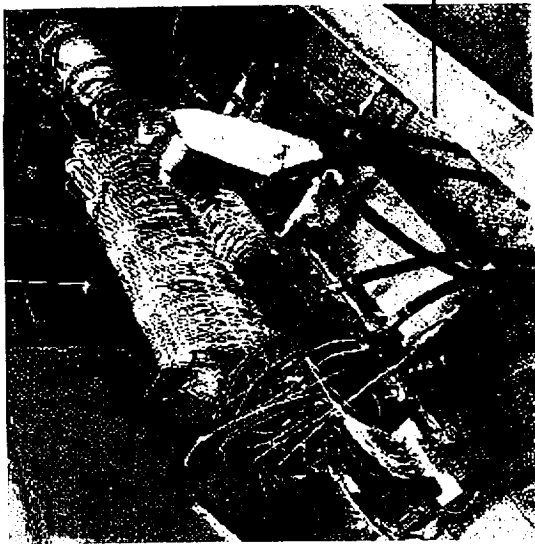
23. Pallix, J. B.; and Copeland, R. A.: Measurement of Catalytic Recombination Coefficients on Quartz Using Laser-Induced Fluorescence. *J. Thermophysics and Heat Transfer*, vol. 10, no. 2, 1996, pp. 224–233.
24. McGrory, W. D.; Slack, D. C.; Applebaum, M. P.; and Walters, R. W.: The General Aerothermodynamic Simulation Program (GASP) Version 2.2, User's Manual. Aerosoft, Inc., 1993.
25. Goulard, R.: On Catalytic Recombination Rates in Hypersonic Stagnation Heat Transfer. *Jet Propulsion*, vol. 28, no. 11, Nov. 1958, pp. 737–745.
26. Park, C.: A Review of Reaction Rates in High Temperature Air. AIAA Paper 89-1740, Buffalo, N.Y., 1989.
27. Yoshikawa, K. K.; and Katzen, E. D.: Charts for Air-Flow Properties in Equilibrium and Frozen Flows in Hypersonic Nozzles. NASA TN D-693, 1961.
28. Pai, S.: *Radiation Gas Dynamics*. Springer-Verlag/Weien, 1966, pp. 188–190.
29. Katzen, E. D.; and Kaattari, G. E.: Inviscid Hypersonic Flow Around Blunt Bodies. *AIAA J.*, vol. 3, no. 7, 1965, pp. 1230–1237.
30. Ames Research Staff: Equations, Tables, and Charts for Compressible Flow. NASA Report 1135, 1953.
31. Stewart, D. A.; and Marvin, J. G.: Convective Heat-Transfer Rates on Large-Angle Conical Bodies. NASA TN D-5526, Nov. 1969.
32. Zoby, E. V.; and Sullivan, E. M.: Effect of Corner Radius on Stagnation Point Velocity Gradients on Blunt Axisymmetric Bodies. NASA TM X-1067, 1966.
33. Rosner, D. E.: Analysis of Air Arc-Tunnel Data. *AIAA J.*, vol. 2, May 1965, pp. 945–948.
34. Powers, C. A.; and Kendall, R. M.: *Aerotherm Chemical Equilibrium Computer Program User's Manual*. Cosmic No. LEW-11722, May 1969.
35. Gupta, R. N.; Thompson, R. A.; and Kam-Pui, L.: A Review of Reaction Rates and Thermodynamic and Transport Properties for an 11-Species Air Model for Chemical and Thermal Nonequilibrium Calculations to 30,000 K. NASA RP-1232, Aug. 1990.
36. Tong, H.: *Non-equilibrium Chemistry Boundary Layer Integral Matrix Procedure*. Acurex Corporation, Mountain View, Calif., Aerotherm Dept. UM-73-37, Apr. 1973.

Table 1. Candidate TPS

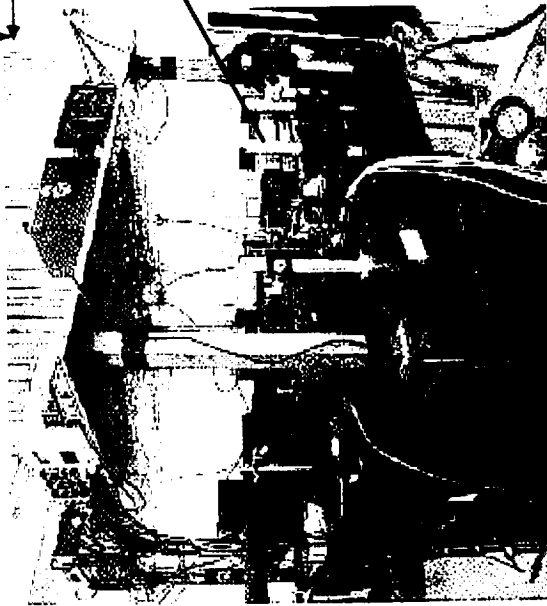
Coating	Substrate	Sample	Test models	Supplier
1. RCG	FRCI-12	Blunt cone/ split tube	Blunt cone/ split tube	NASA/ARC
2. TUF1	AETB-12	Blunt cone/ split tube	Blunt cone/ split tube	NASA/ARC
3. SIRCA	FRCI-15	Blunt cone	Blunt cone	NASA/ARC
4. None	TABI	Disk/cloth	F-F cylinder/ tube liner	NASA/ARC
5. Grey C-9	Nextel 440	Disk/cloth	F-F cylinder/ tube liner	Rockwell International Corp.
6. PCC	Nextel 440	Disk/cloth	F-F cylinder/ tube liner	NASA/ARC
7. None	Nextel 440	Cloth	Tube liner	NASA/ARC
8. C-CAT	Reinforced carbon-carbon	Disk	F-F cylinder	NASA/LRC
9. LVP	Reinforced carbon-carbon	Disk	F-F cylinder	NASA/LRC
10. ORCC (RT-4)	Reinforced carbon-carbon	Disk/split tube	F-F cylinder	ROHR
11. None	SiC/SiC	Disk	F-F cylinder	McDonnell Douglas Aerospace
12. Russian	Reinforced carbon-carbon	Disk	F-F cylinder	McDonnell Douglas Aerospace
13. None	Inconel 617	Disk/sheet	F-F cylinder/ tube liner	McDonnell Douglas Aerospace
14. Oxide	Inconel 617	Disk/sheet	F-F cylinder/ tube liner	McDonnell Douglas Aerospace
15. Oxide	PM-1000 (nickel-based)	Disk/sheet	F-F cylinder	ROHR
16. Oxide	MA-956 (iron-based)	Disk/sheet	F-F cylinder	ROHR

Table 2. Typical arc-jet operating conditions

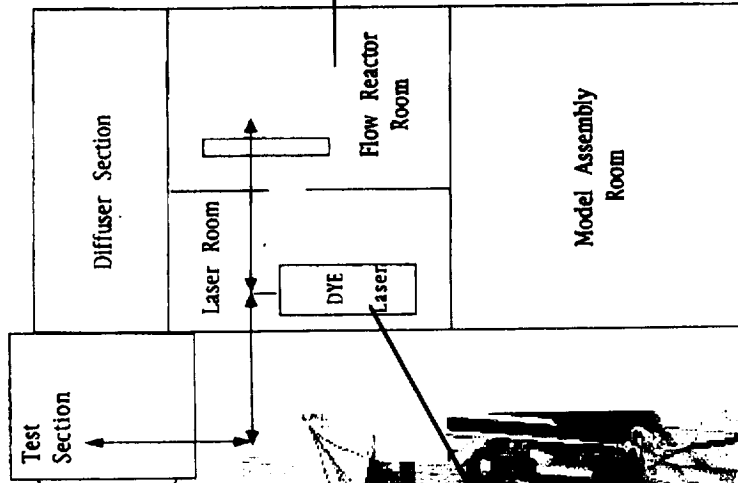
Test case	Power, MW	Mass flow, gm/s	Pressure, atm	Enthalpy, MJ/kg Bulk/Effective
Nitrogen				
1	1.12	23.6	0.68	12.4/13.2
2	2.8	45.4	1.36	18.0/20.3
3	4.2	69.4	2.04	19.6/20.9
4	5.44	101.2	2.72	19.1/19.8
Air				
1	1.04	23.6	0.68	12.1/13.9
2	2.52	45.4	1.36	17.5/18.8
3	5.0	101.2	2.72	17.1/19.8
4	7.2	157.9	4.08	16.9/18.6



(a) Arc-Heater



(b) Laser

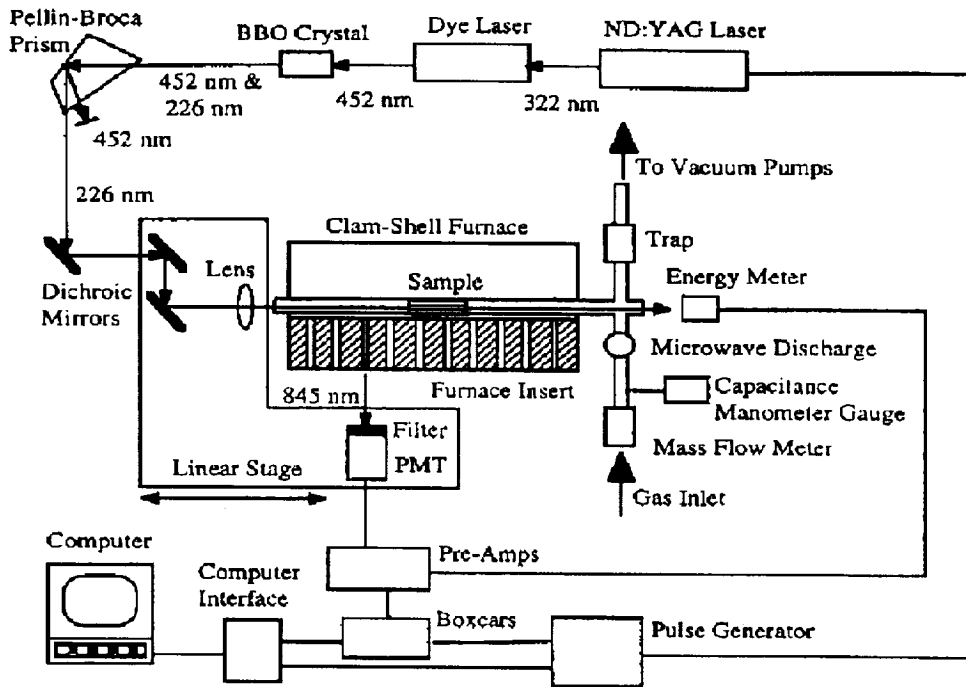


Sketch of complex

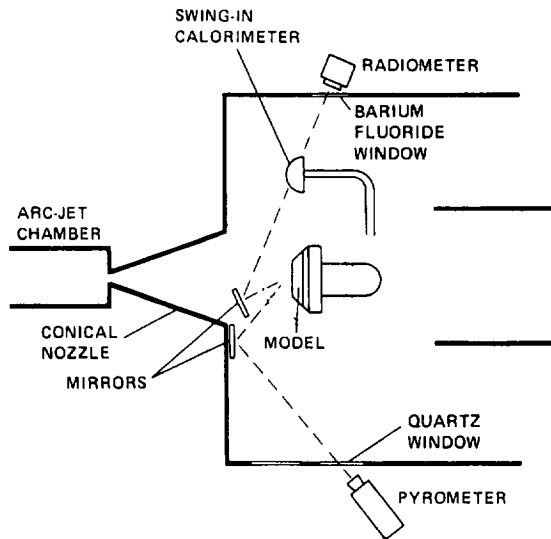


(c) Flow Reactor/Side-Arm Reactor

Figure 1. LASER complex.

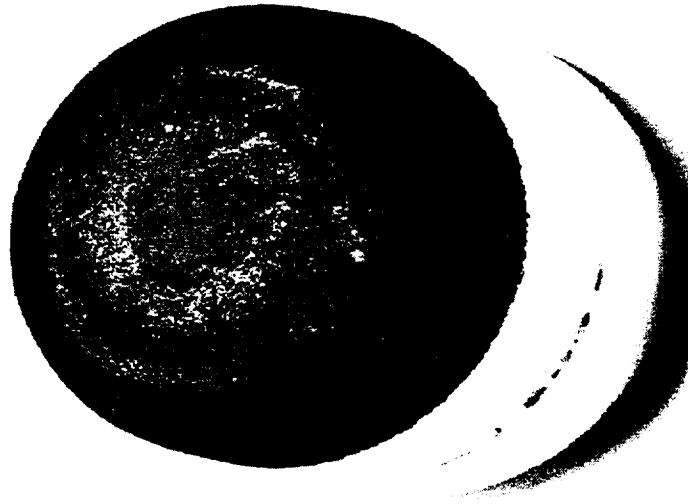


(a) Side-arm reactor

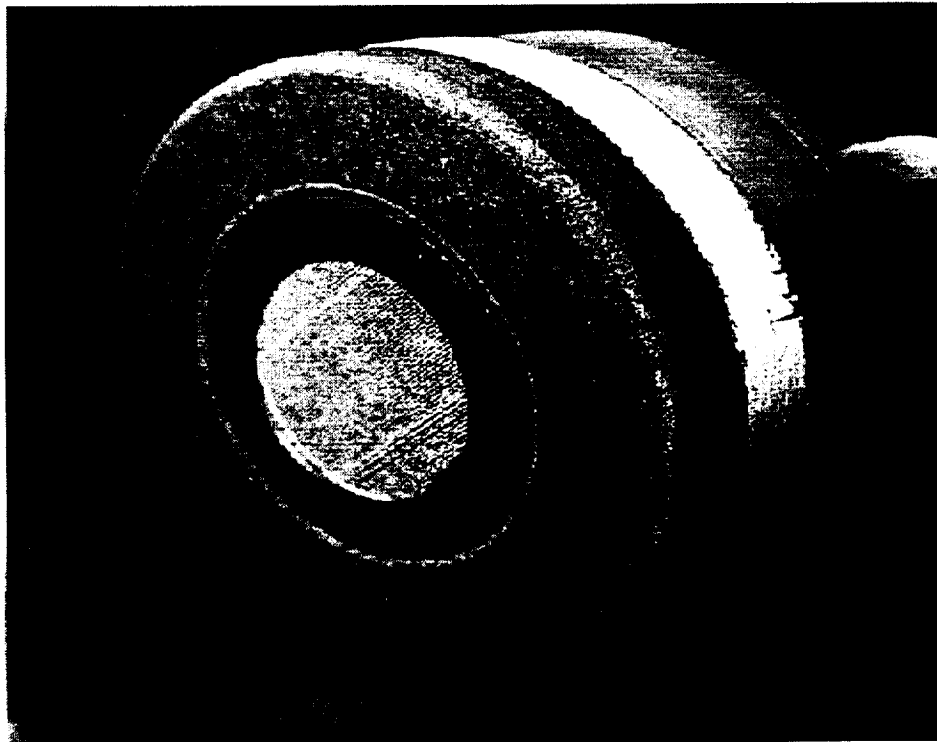


(b) Aerothermodynamic heating facility

Figure 2. Schematics of facility equipment.

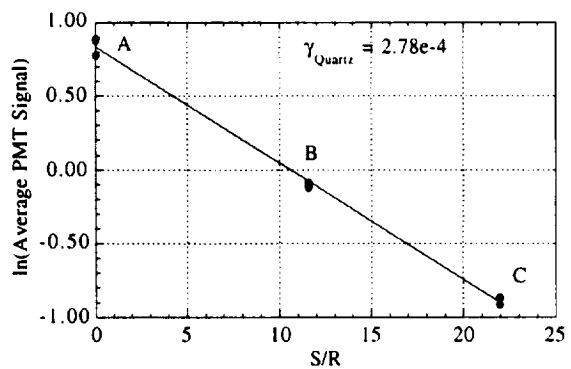
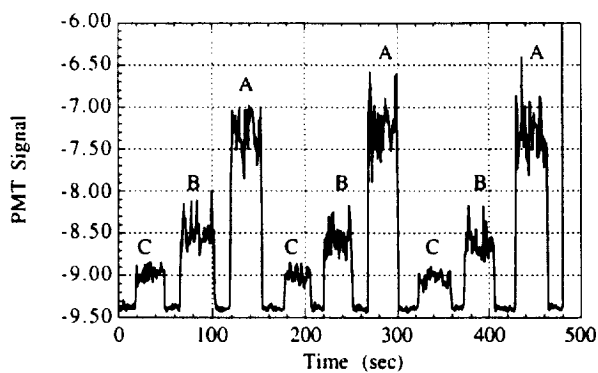


*(a) Conical sample*

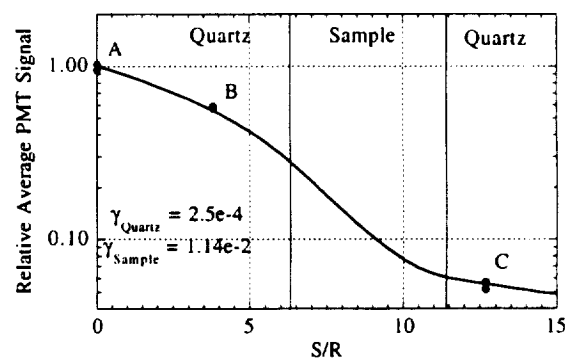
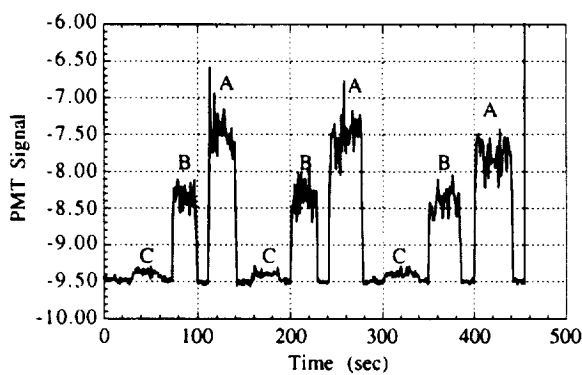


*(b) Cylindrical sample holder*

*Figure 3. Test models.*

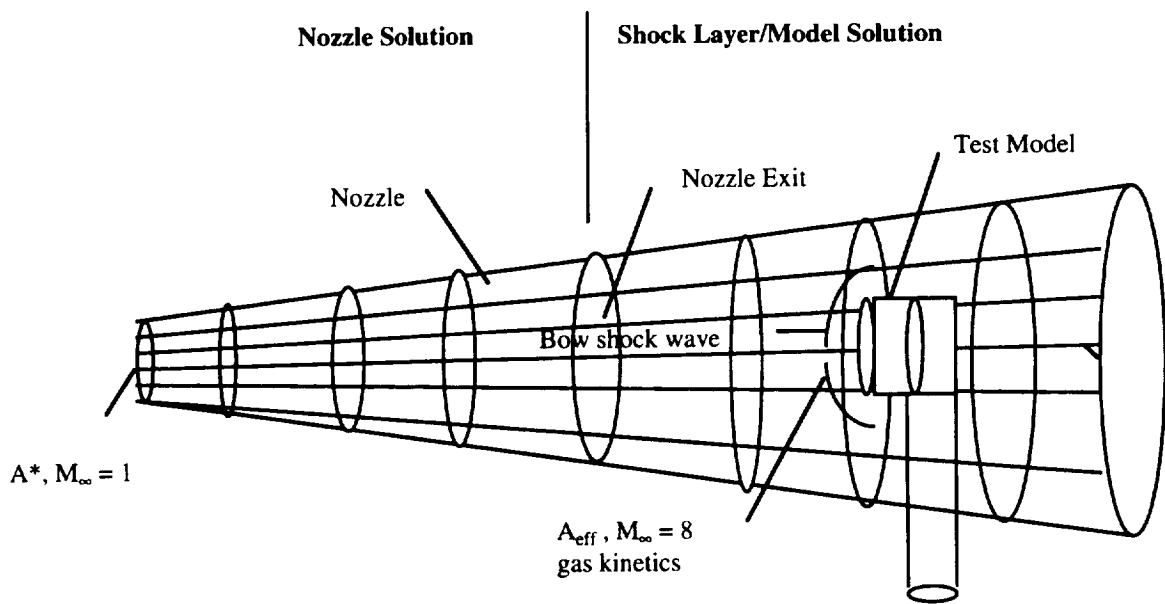


(a) Low catalytic efficiency sample, long tube

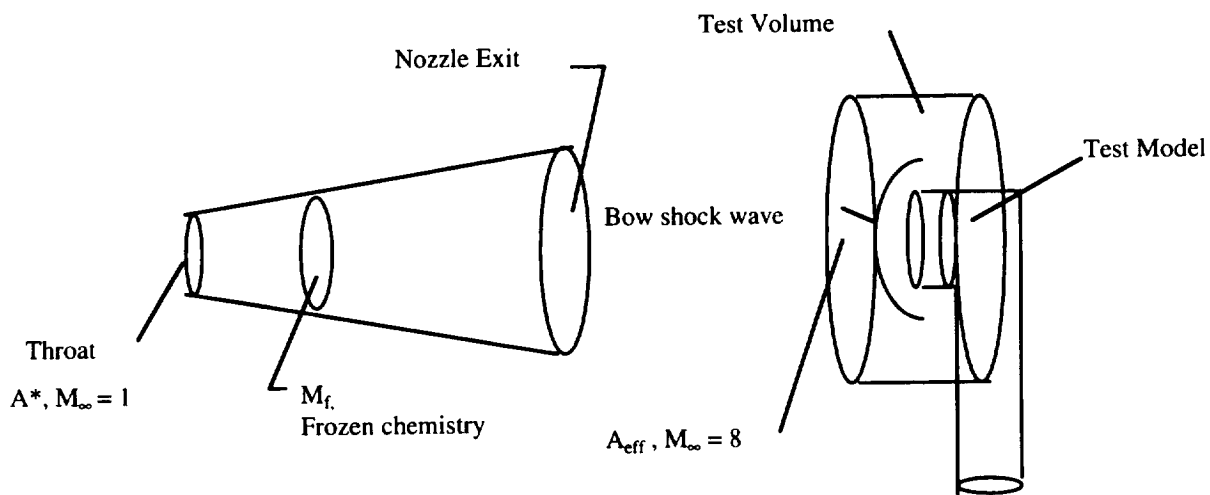


(b) Medium to high catalytic efficiency sample, composite tube section

Figure 4. Typical fluorescence (PMT) signal distribution along diffusion tube in side-arm reactor.

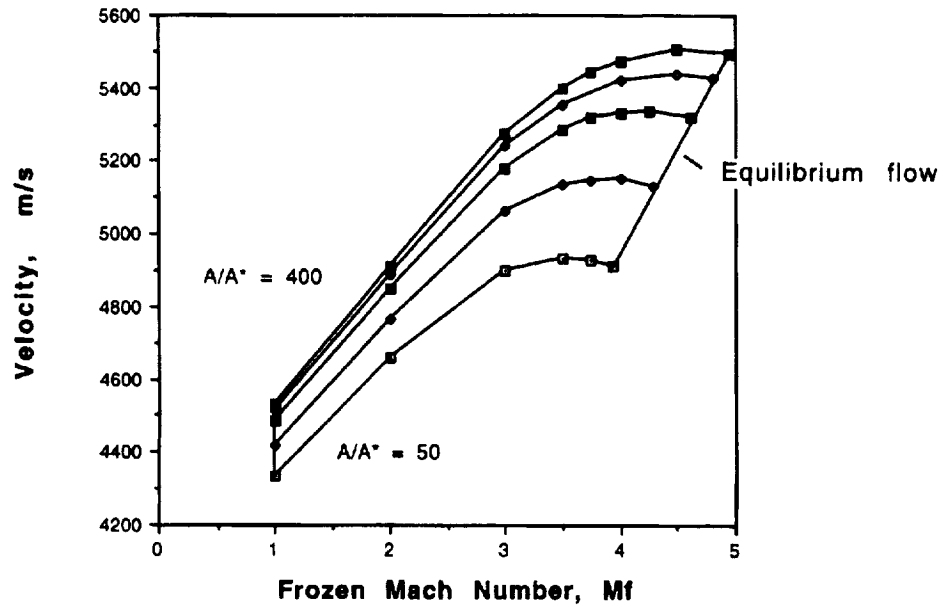


(a) Typical axisymmetric grid for Navier-Stokes computation using GASP

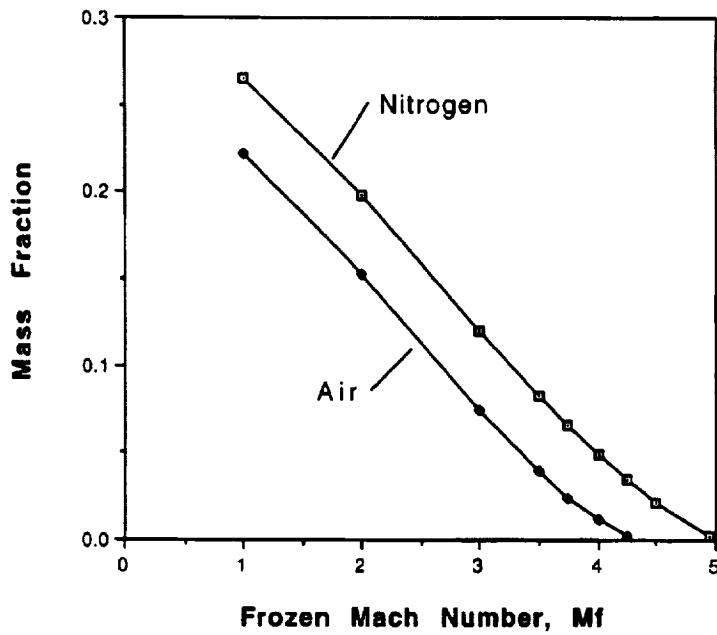


(b) Frozen Mach number flow computation using effective area ratio

Figure 5. Control volume for free-stream and shock layer simulations.

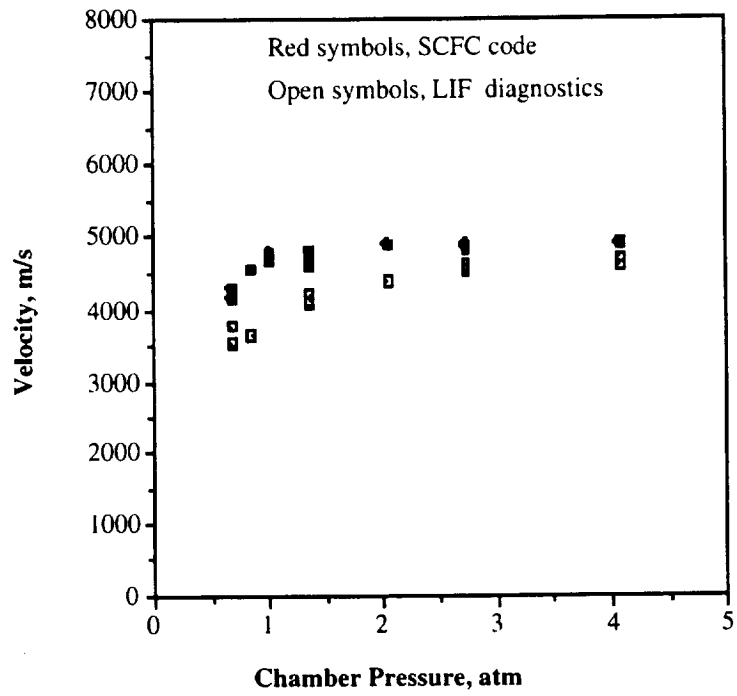


(a) Free-stream velocity in nitrogen ( $H_{e0} = 19 \text{ MJ/kg}$ ,  $P_{ch} = 4.08 \text{ atm}$ )

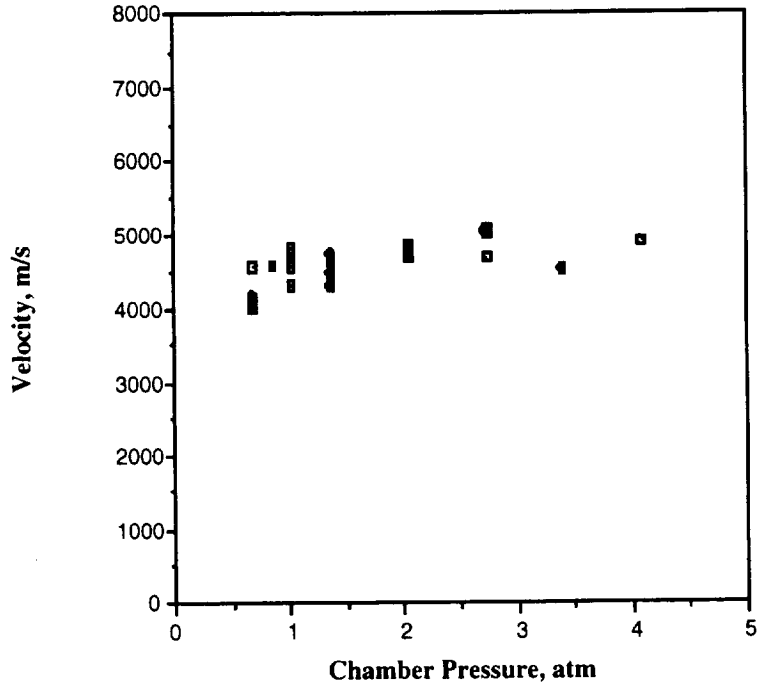


(b) Atomic nitrogen in free stream of arc-jet flow

Figure 6. Predicted free-stream properties relative to frozen Mach number.

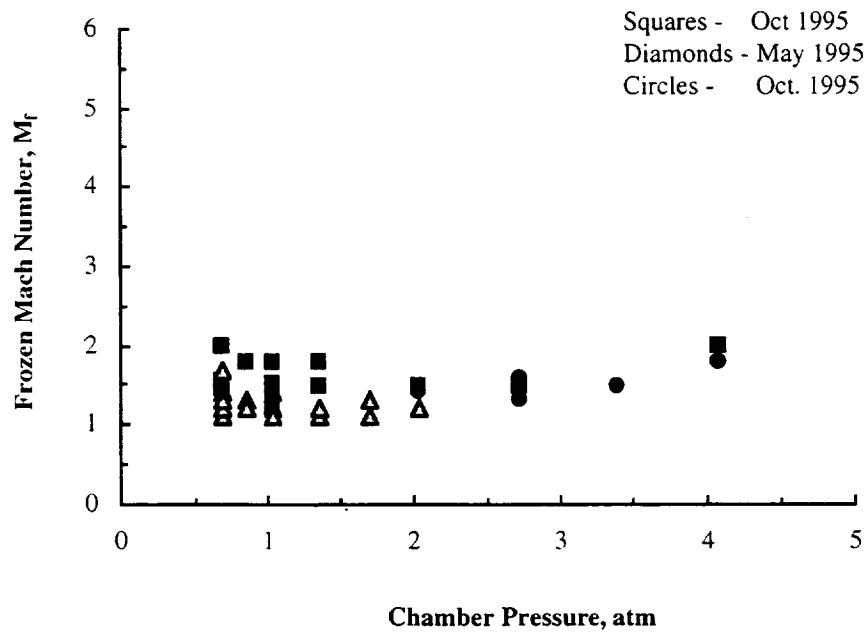


(a) Air

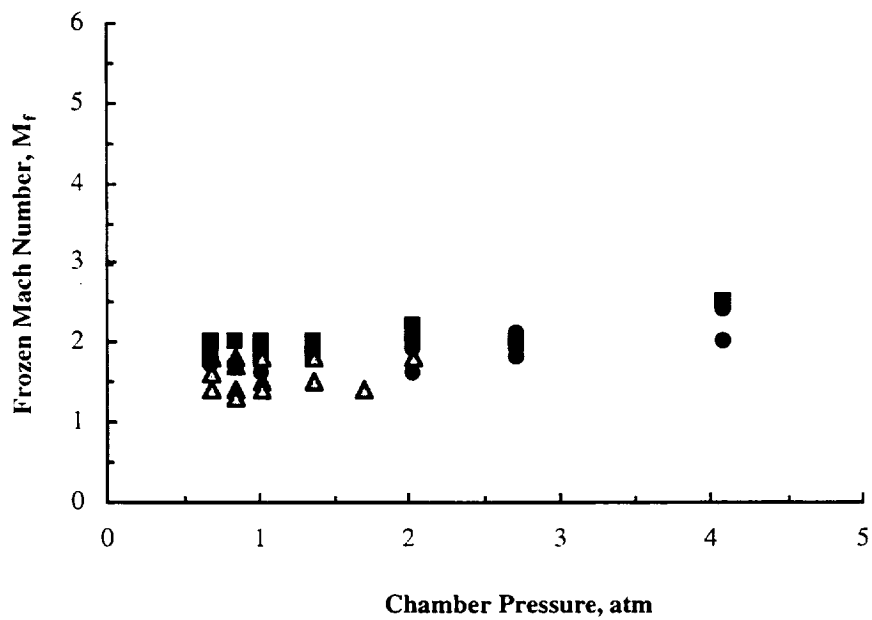


(b) Nitrogen

Figure 7. Comparison between predicted and calculated velocities in nitrogen streams.

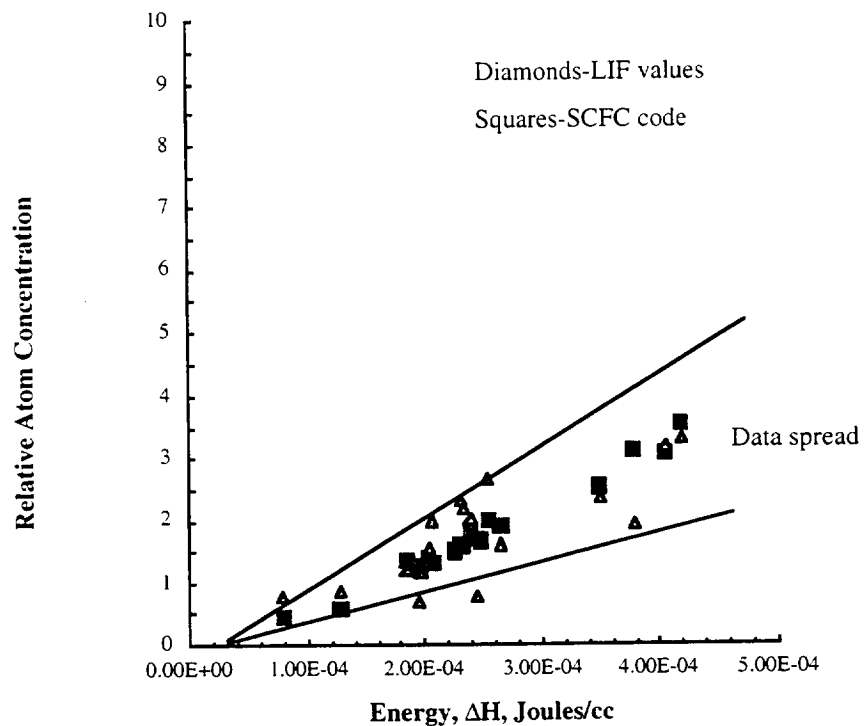


(a) Nitrogen

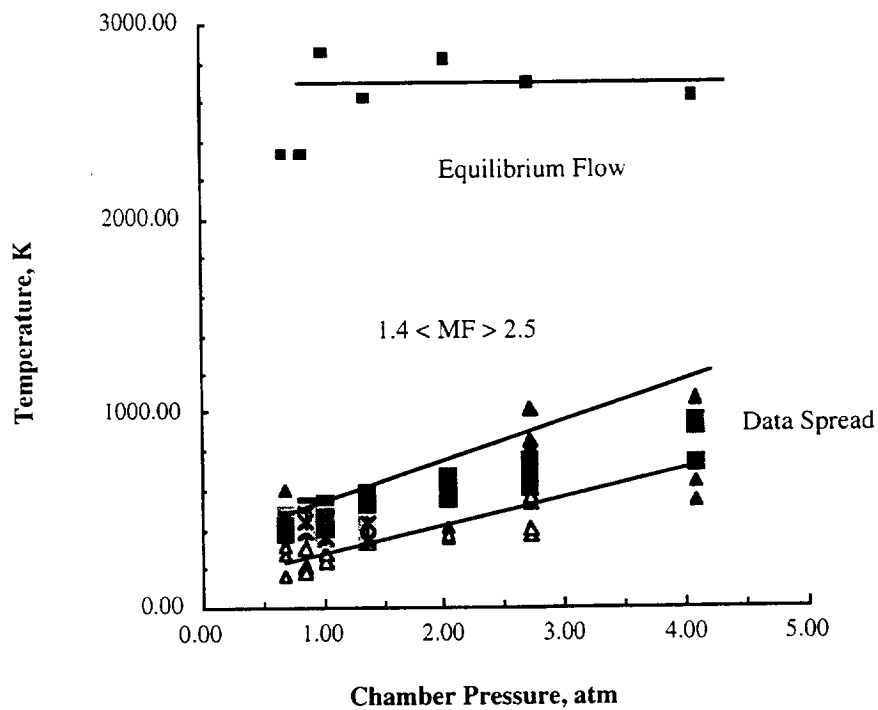


(b) Air

Figure 8. Typical variation in frozen Mach number during arc-jet tests.



(a) Relative nitrogen atom concentration



(b) Free-stream temperature

Figure 9. Variation of stream properties in the AHF during surface catalysis studies.

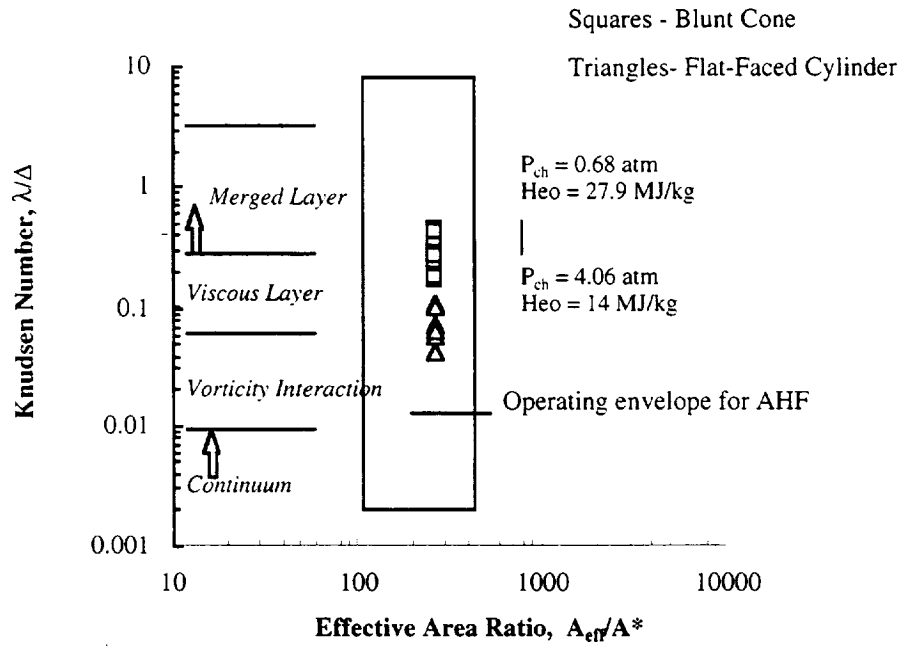


Figure 10. Flow field in front of arc-jet test models during exposures to air.

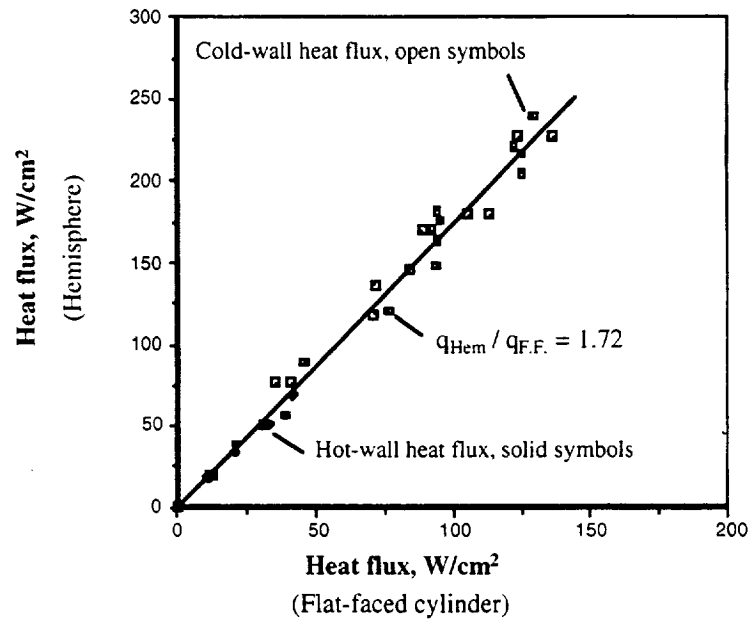
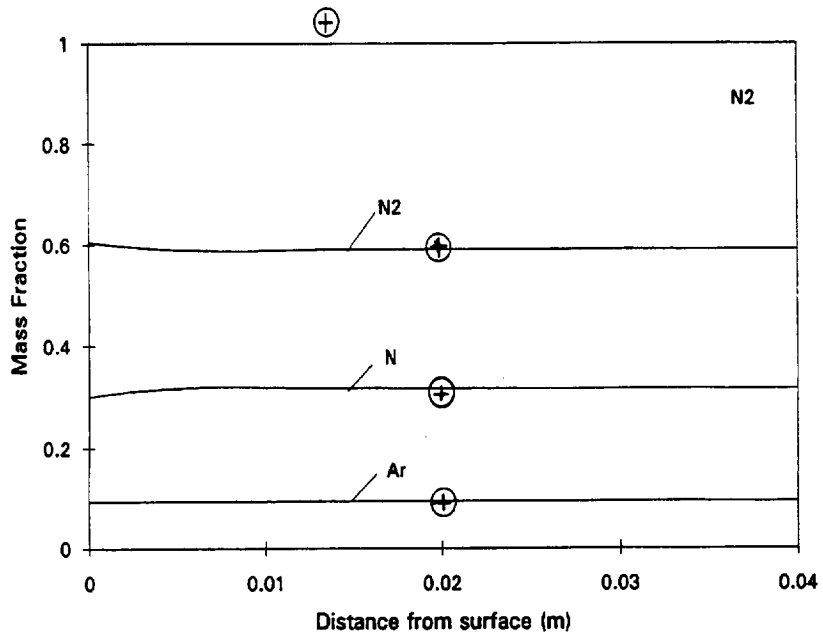
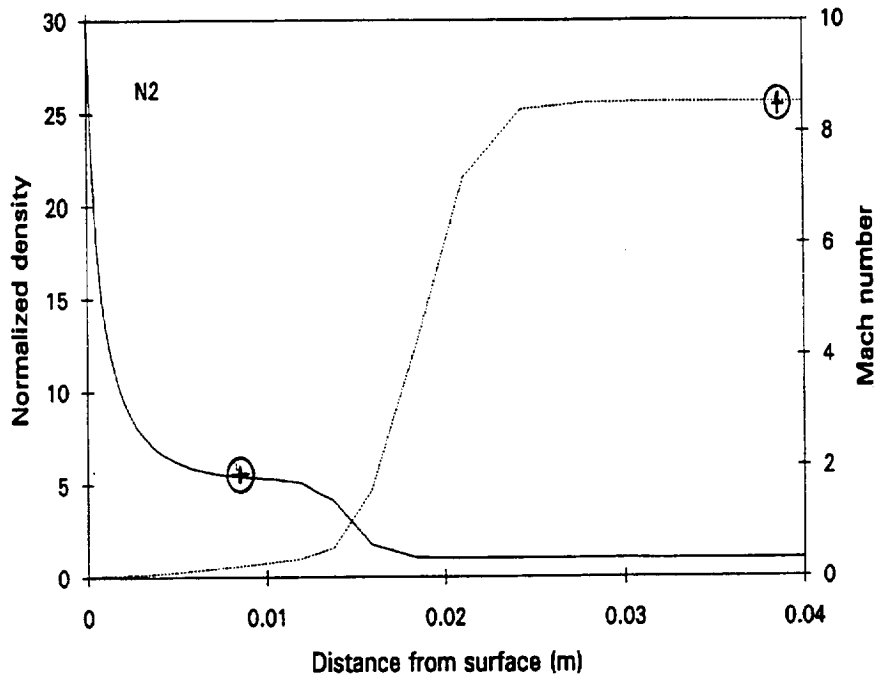


Figure 11. Correlation of stagnation point heat flux between hemisphere and flat-faced cylinder.

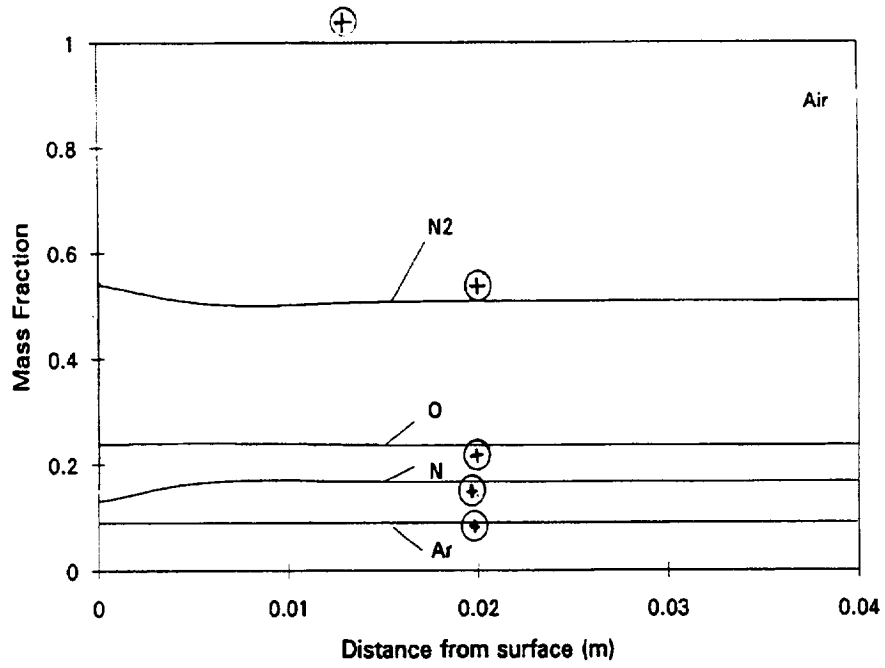


(a) Species concentration profiles

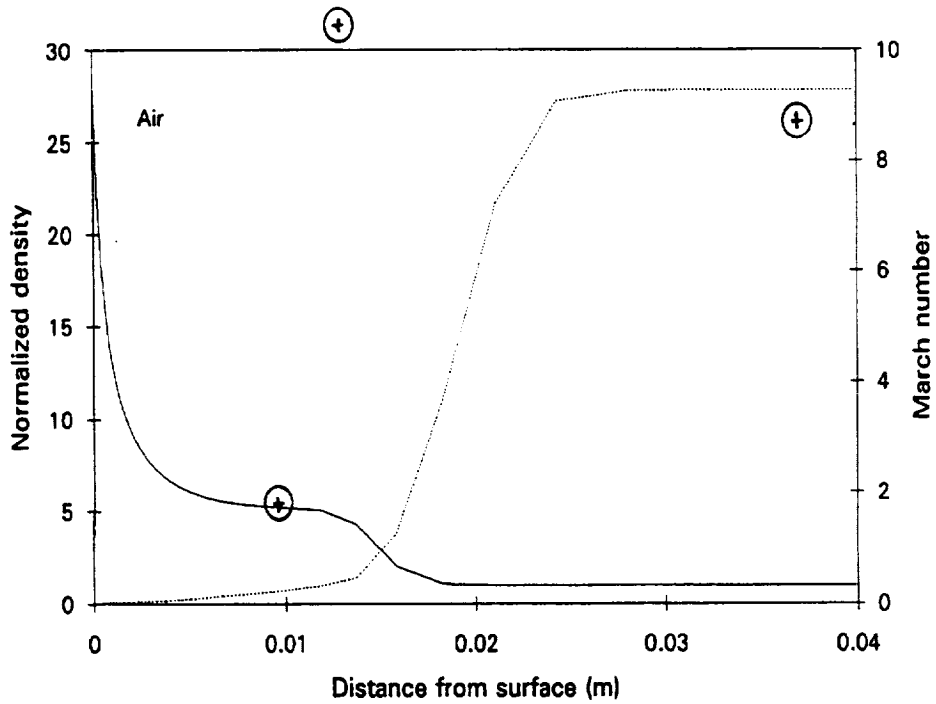


(b) Density and Mach number profiles

Figure 12. Comparison of predicted flow properties using SCFC and GASP solutions (nitrogen, test case 2).

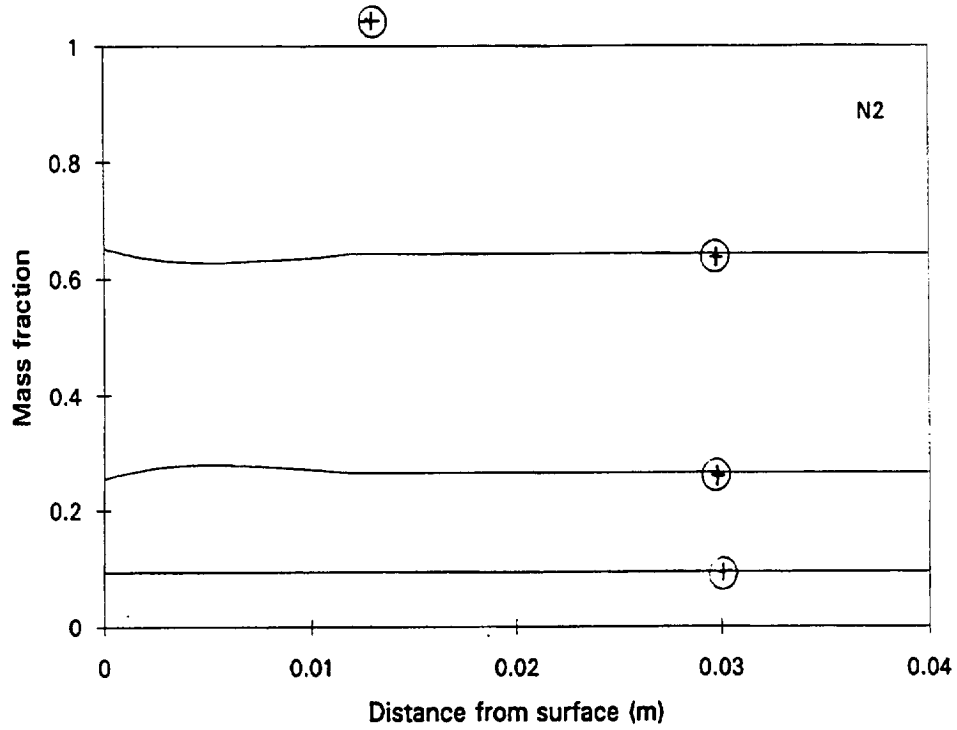


(a) Species concentration profiles

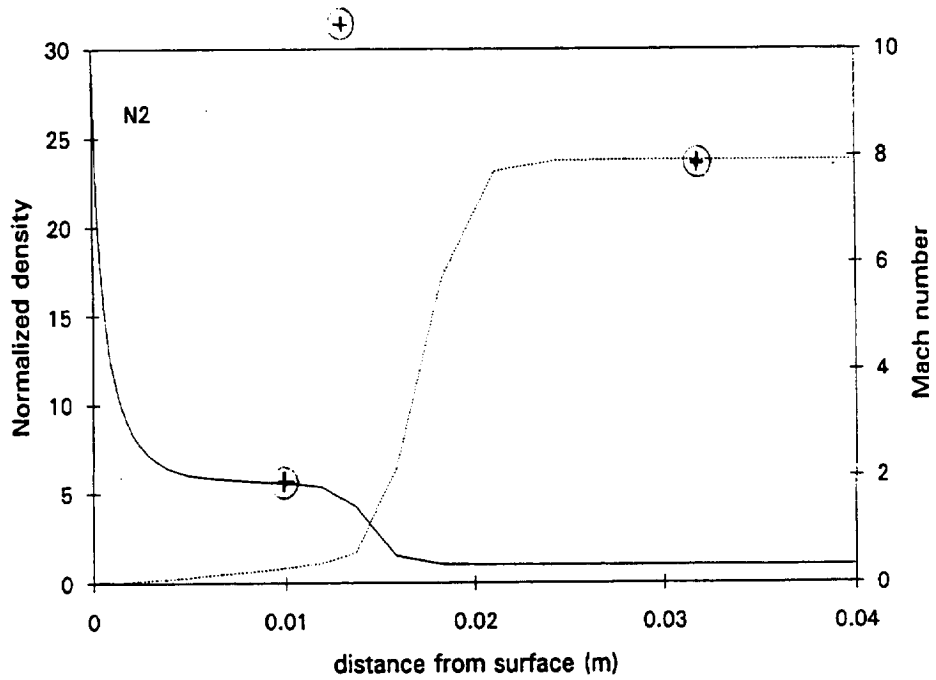


(b) Density and Mach number profiles

Figure 13. Comparison of predicted flow properties using SCFC and GASP solutions (air, test case 2).

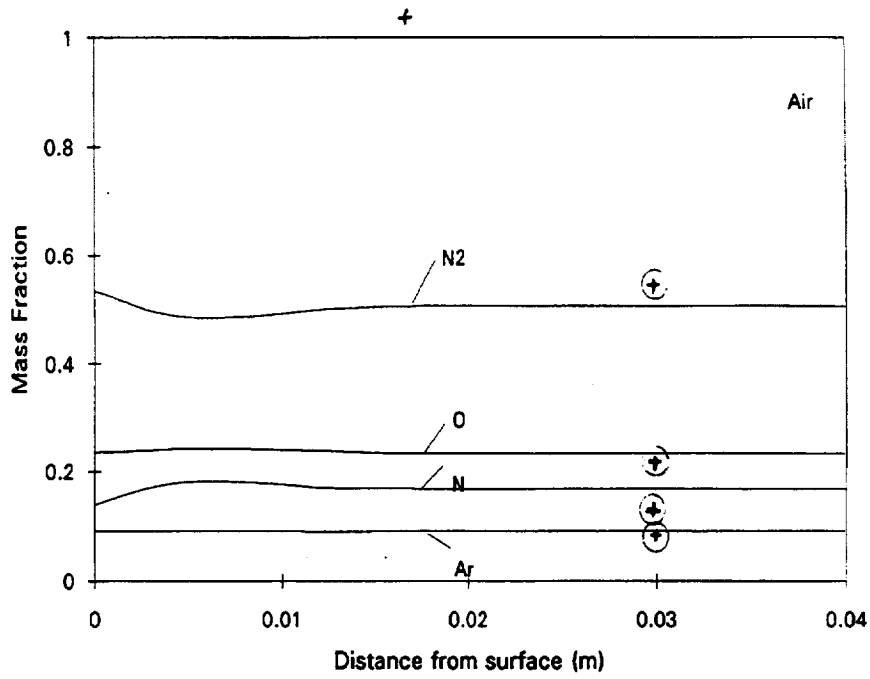


(a) Species concentration profiles

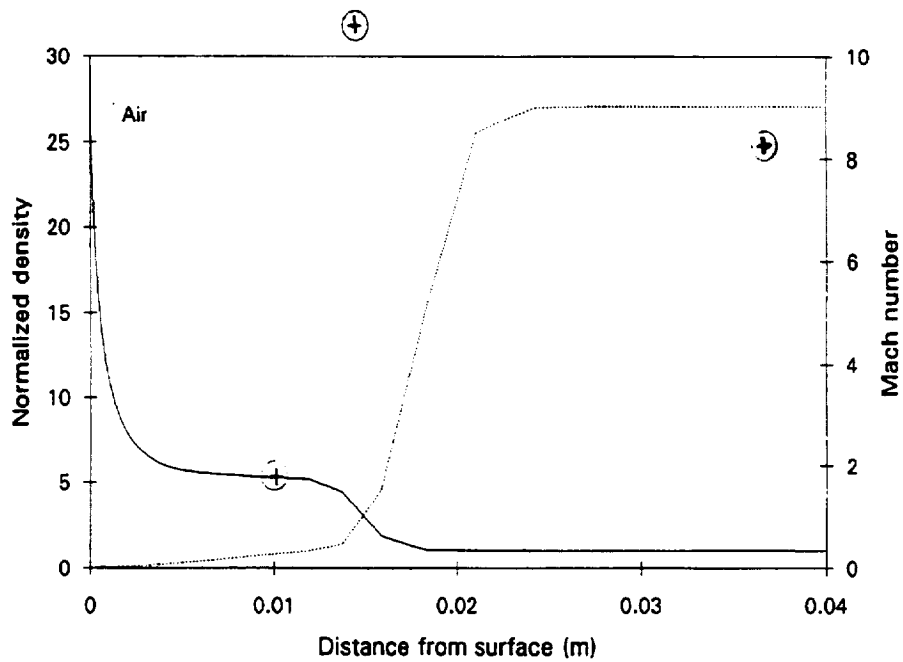


(b) Density and Mach number profiles

Figure 14. Comparison of predicted flow properties using SCFC and GASP solutions (nitrogen, test case 4).

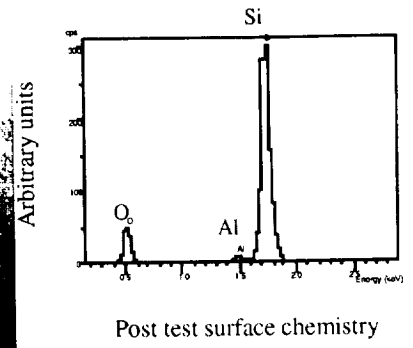
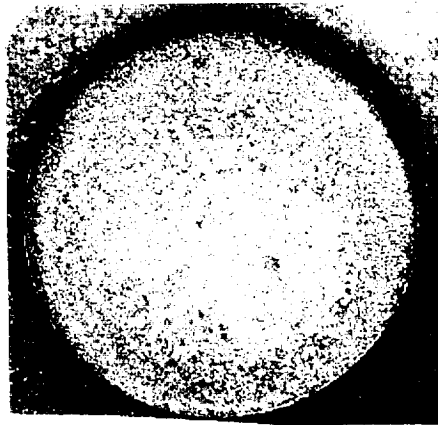
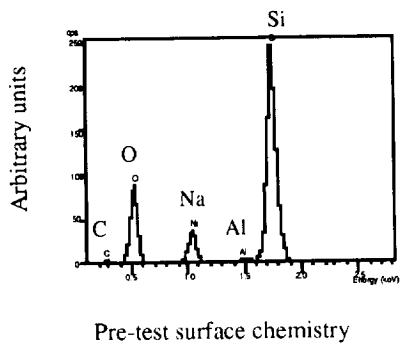


(a) Species concentration profiles

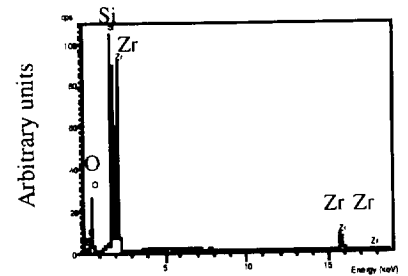
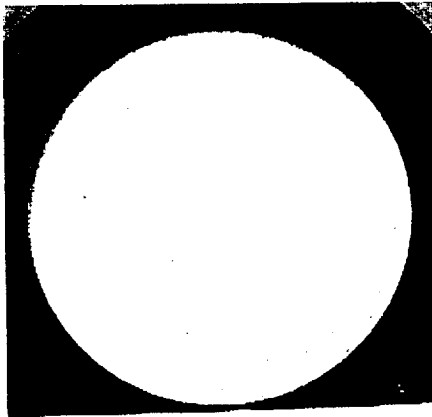
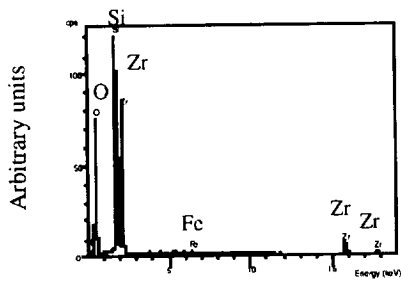


(b) Density and Mach number profiles

Figure 15. Comparison of predicted flow properties using SCFC and GASP solutions (air, test case 3).



(a) C-CAT coated ACC



(b) LVP coated ACC

Figure 16. Pre- and posttest photographs and surface chemistry of coated ACC.

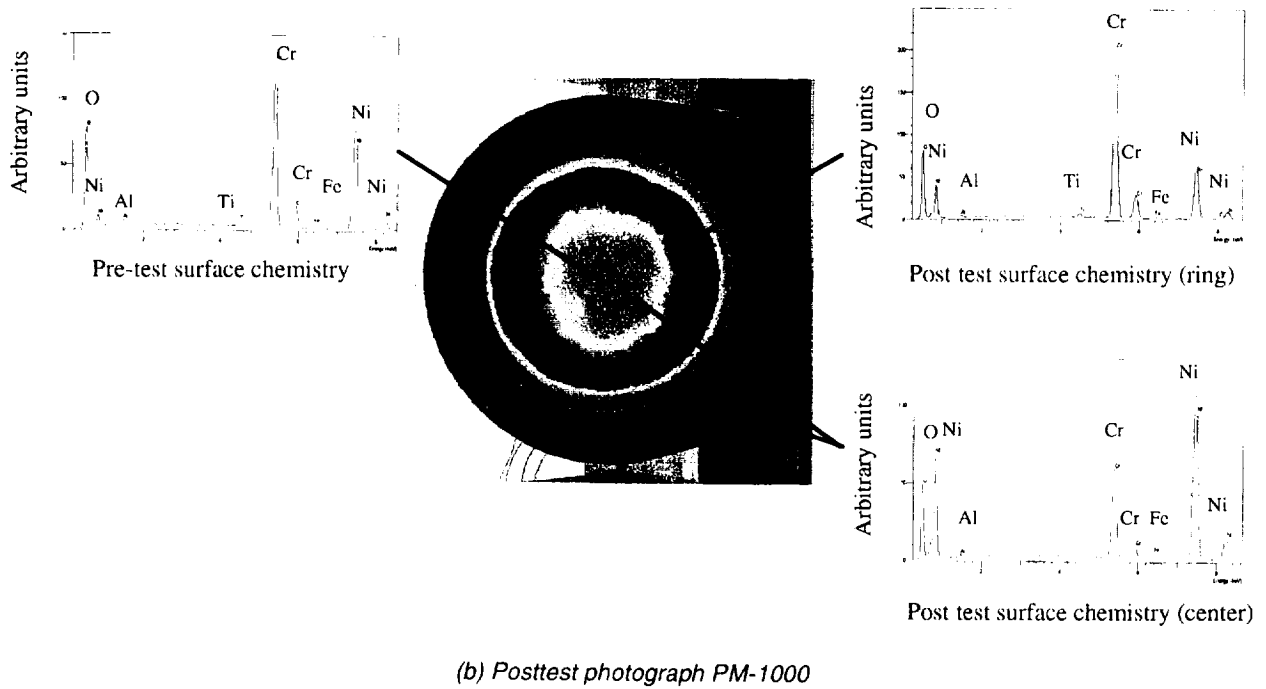
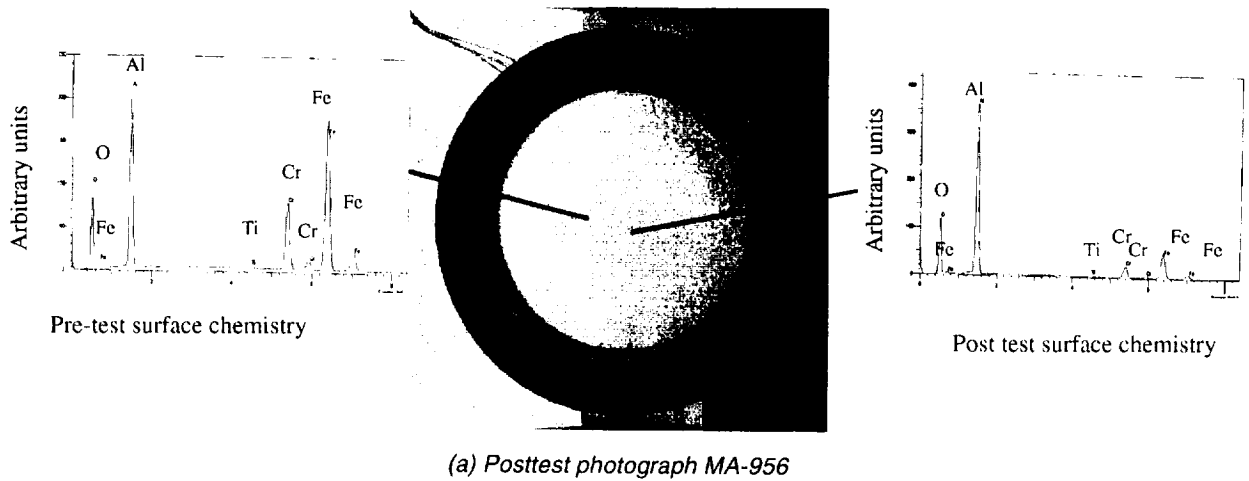
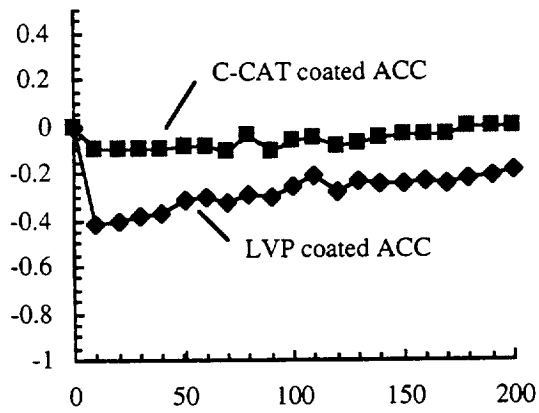
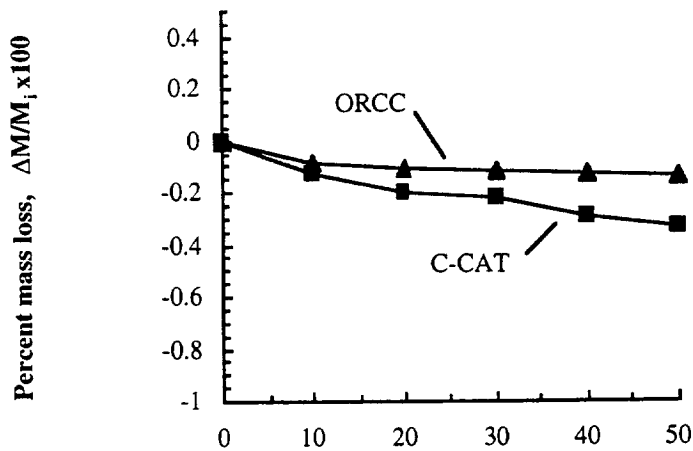


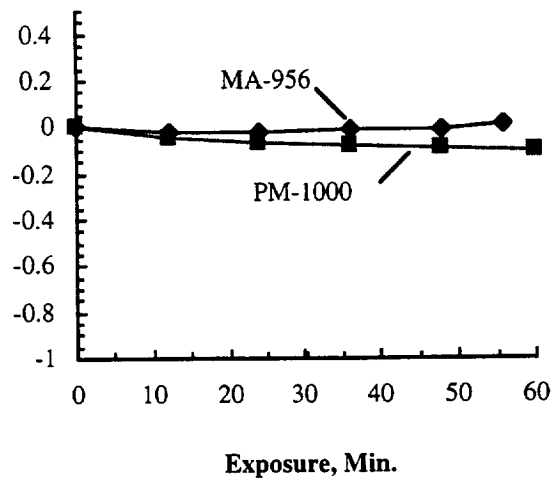
Figure 17. Pre- and posttest photographs and surface chemistry of metallic TPS.



(a) ACC mass loss,  $T_w = 1367\text{ K}$

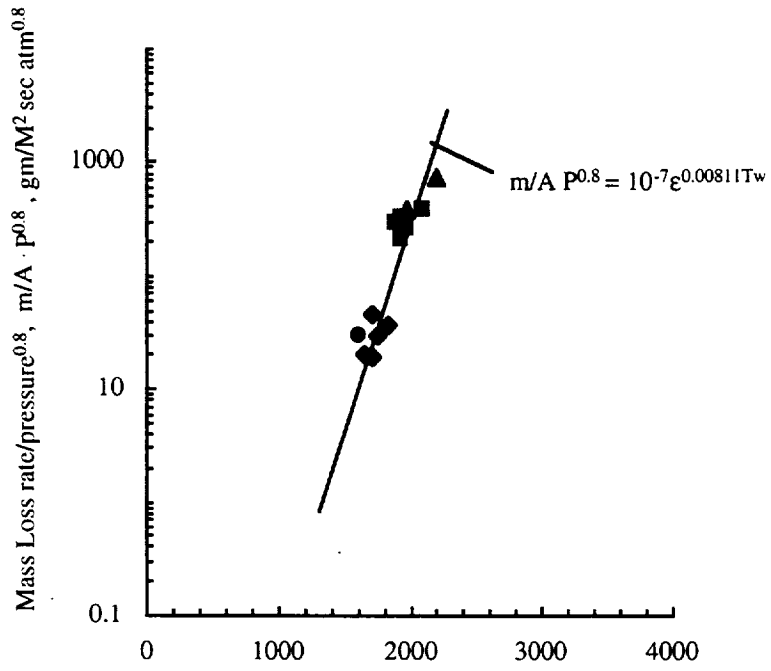


(b) ACC mass loss,  $T_w = 1644\text{ K}$

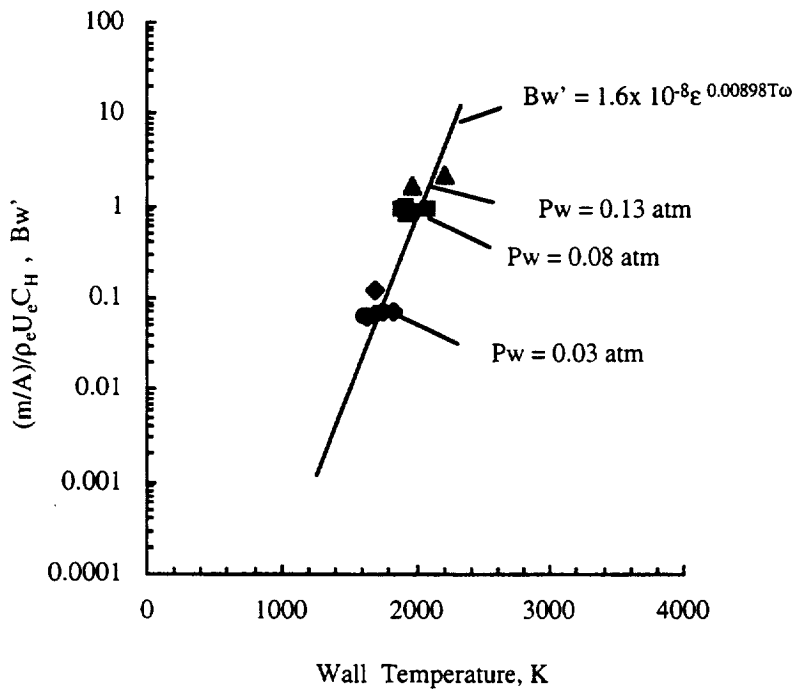


(c) Pre-oxidized metals,  $T_w = 1478\text{ K}$

Figure 18. Mass loss history of candidate SSTO TPS samples during arc-jet exposure in air.



(a) Mass loss rate



(b) Dimensionless mass transfer rate

Figure 19. Mass loss characteristics of SIRCA during arc-jet exposure in air.

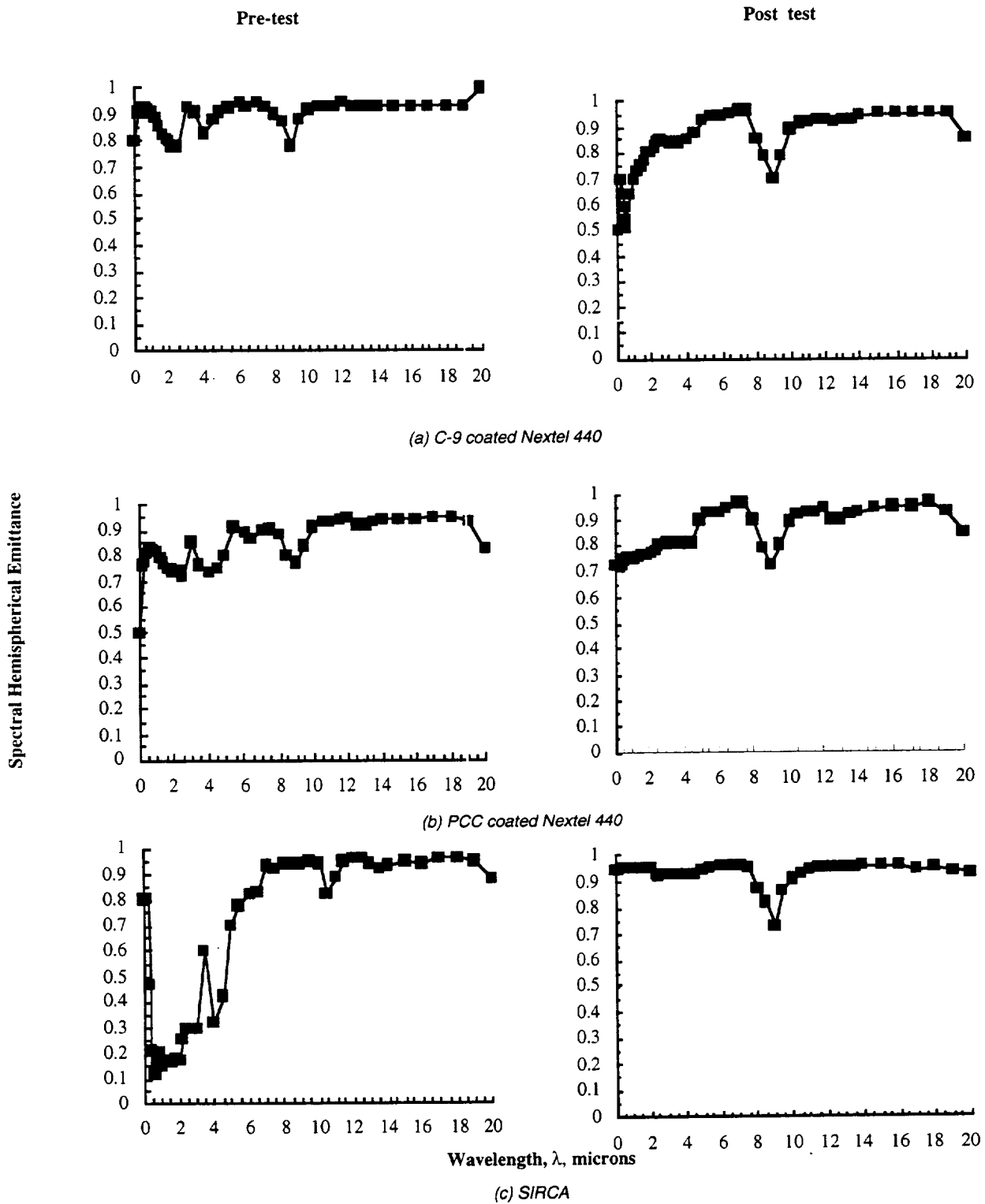


Figure 20. Effect of arc-jet exposure on spectral emittance of fibrous TPS.

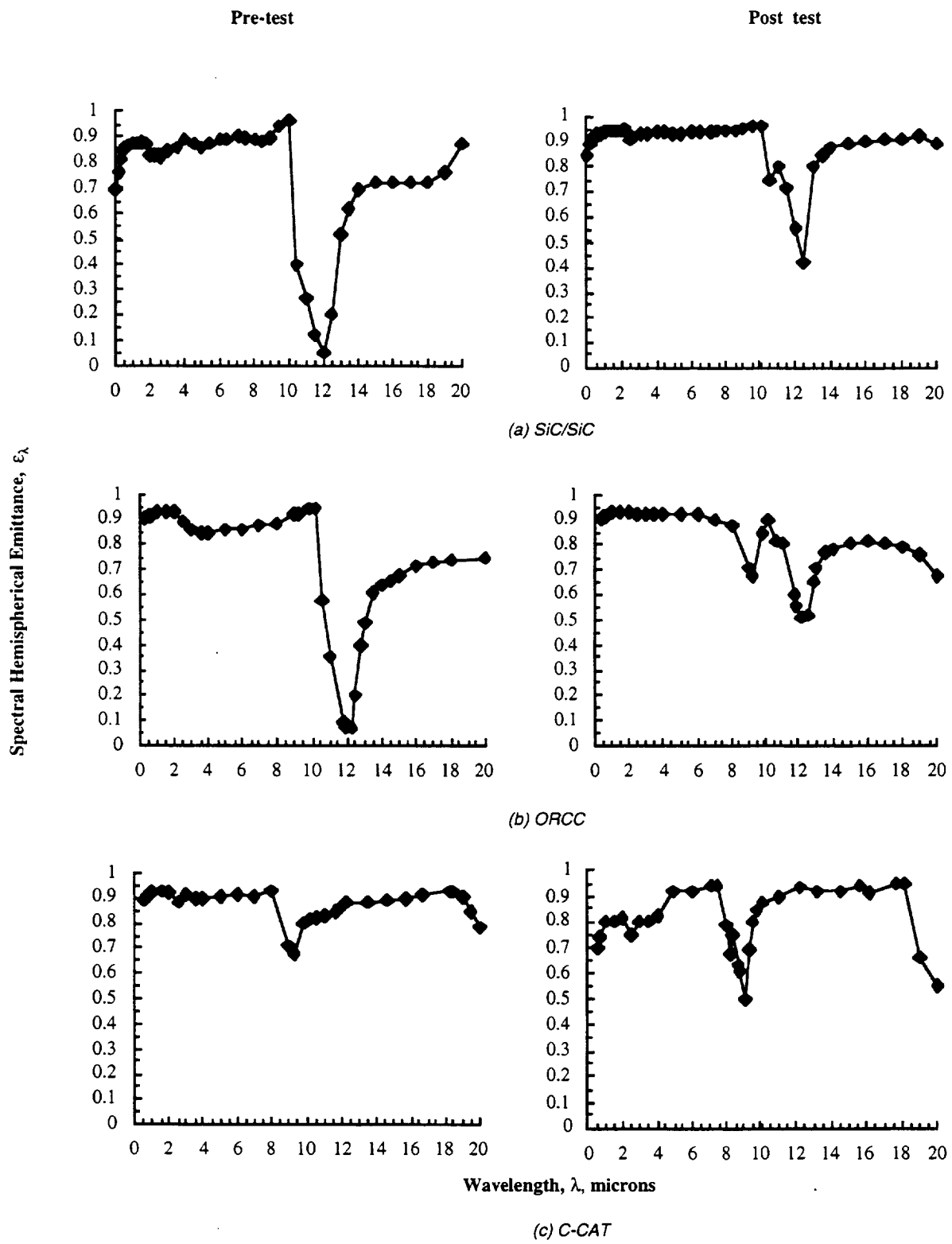


Figure 21. Effect of arc-jet exposure on spectral emittance of carbon composite TPS.

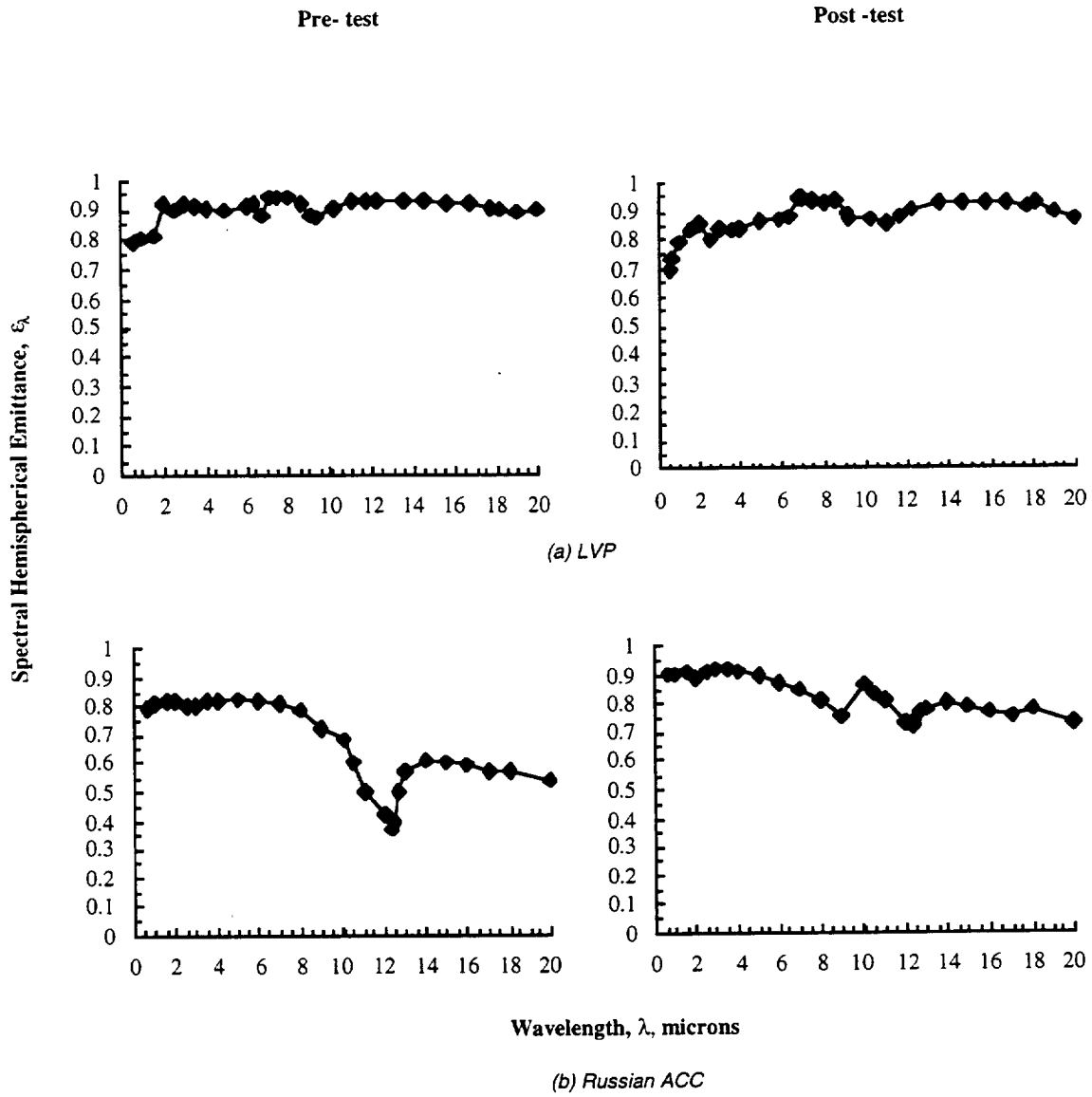


Figure 22. Effect of arc-jet exposure on spectral emittance of carbon composite TPS.



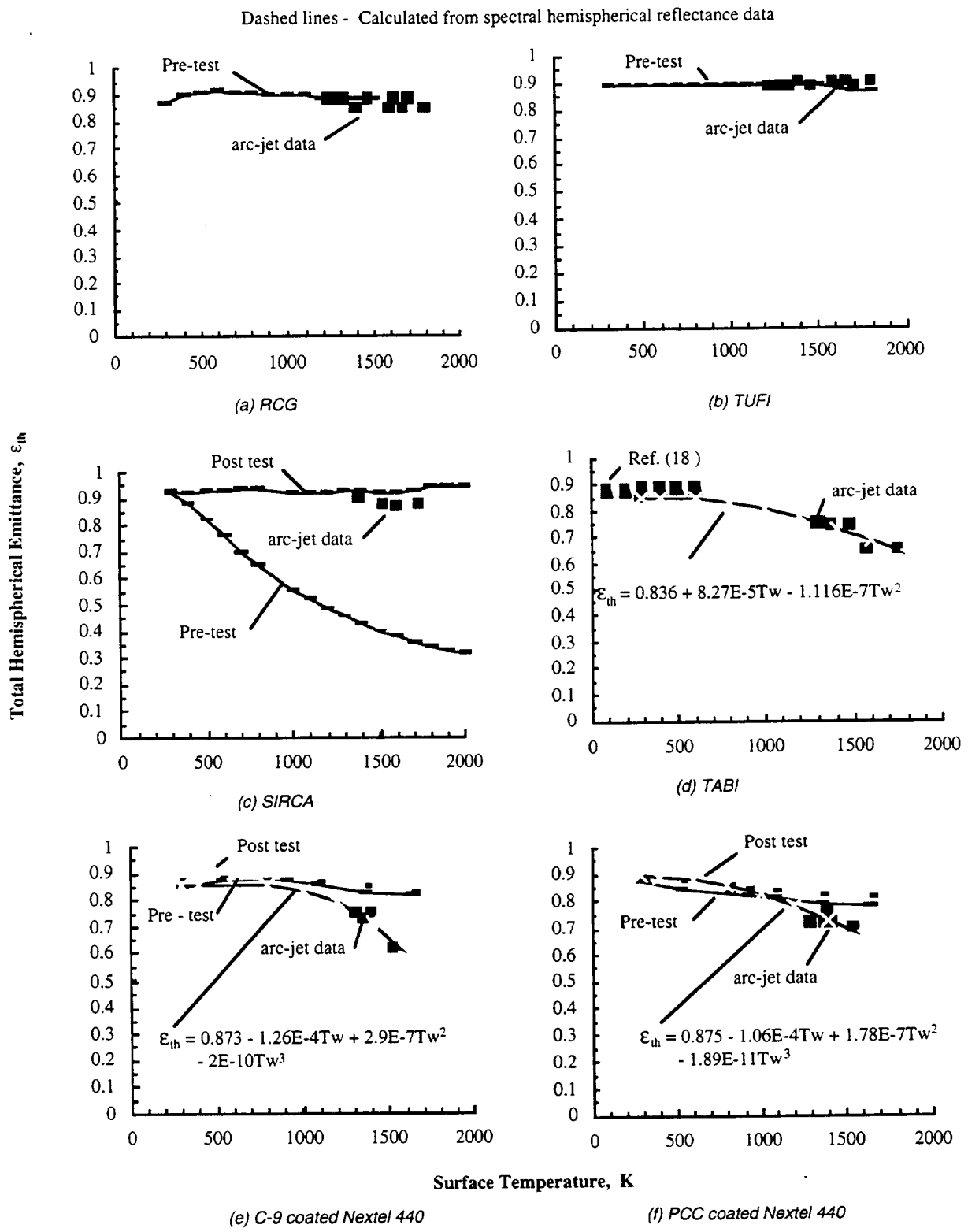


Figure 24. Total hemispherical emittance of fibrous TPS.

Dashed lines - calculated from room temperature spectral reflectance data

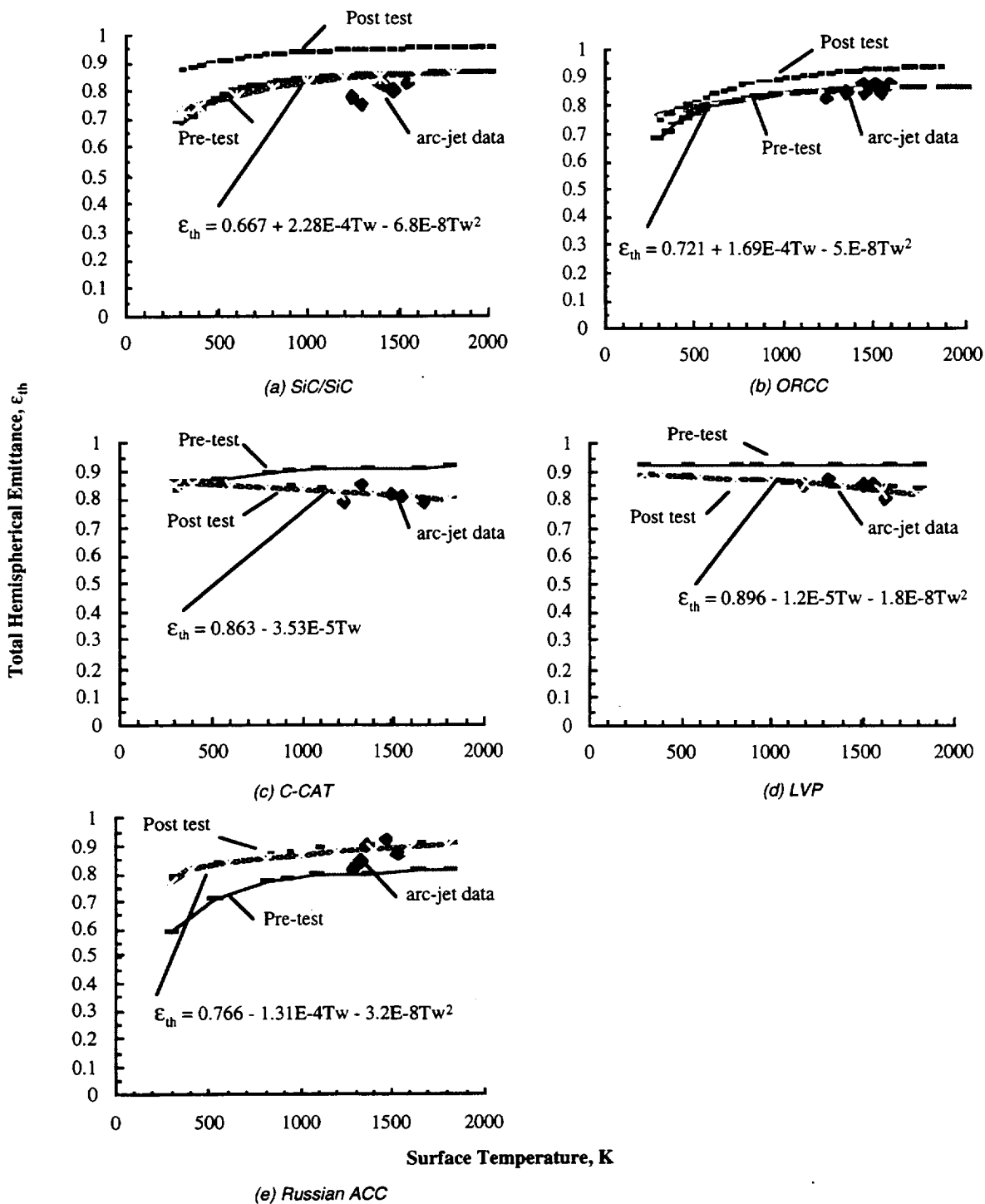


Figure 25. Total hemispherical emittance of carbon composite TPS.

Dashed lines - Calculated from room temperature spectral reflectance data

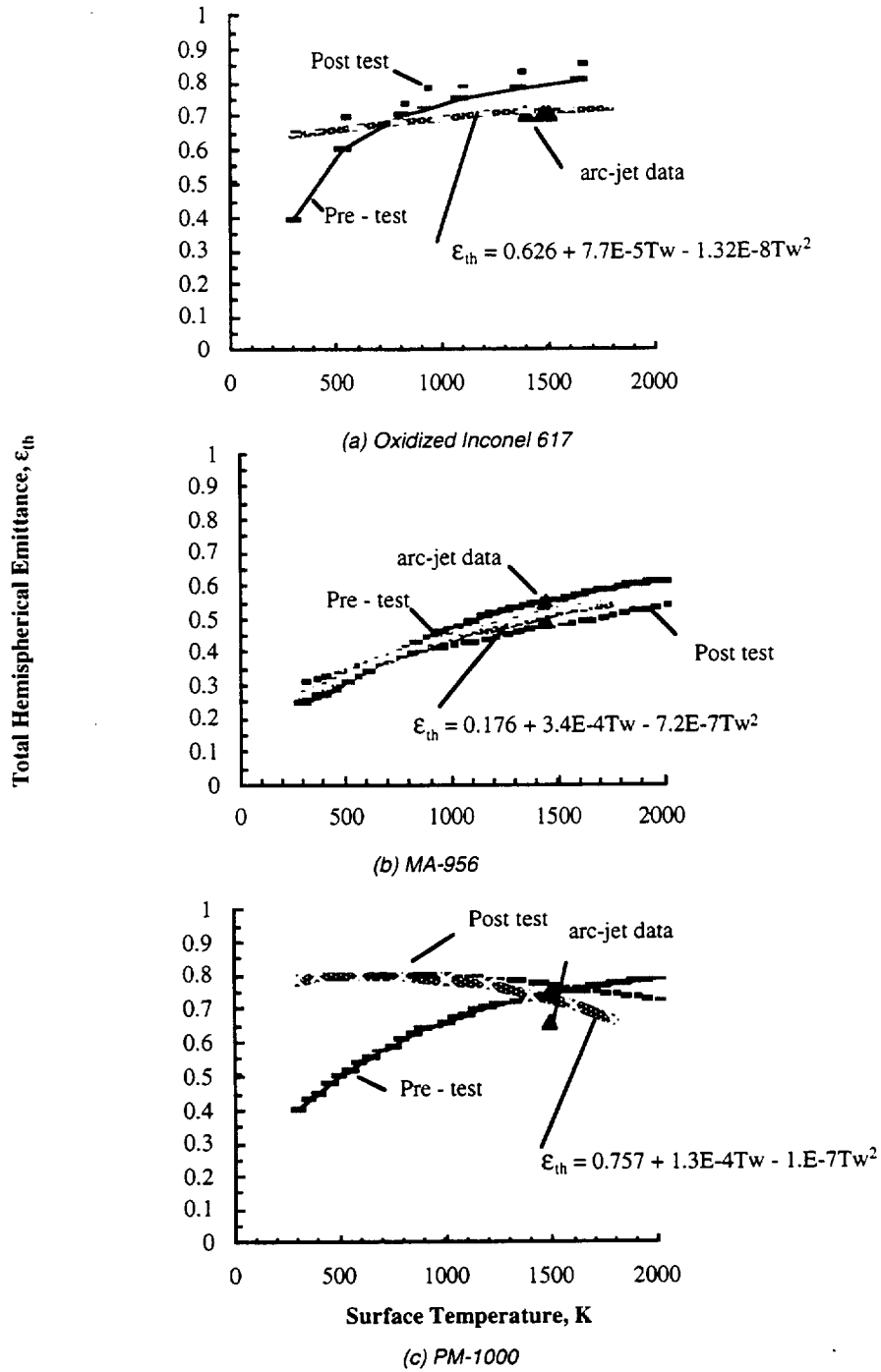


Figure 26. Total hemispherical emittance of metallic TPS.

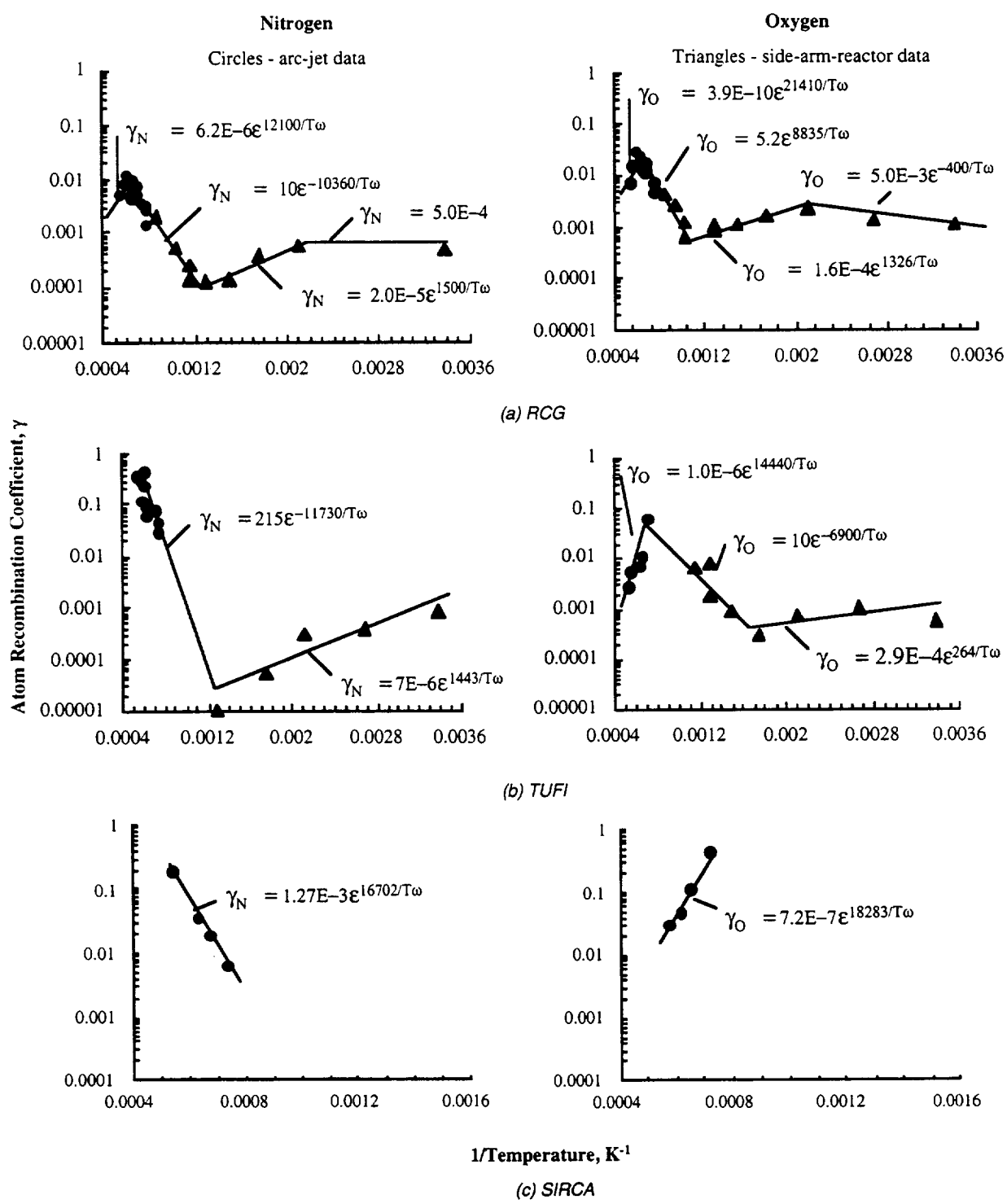


Figure 27. Atom recombination coefficients for rigid fibrous TPS.

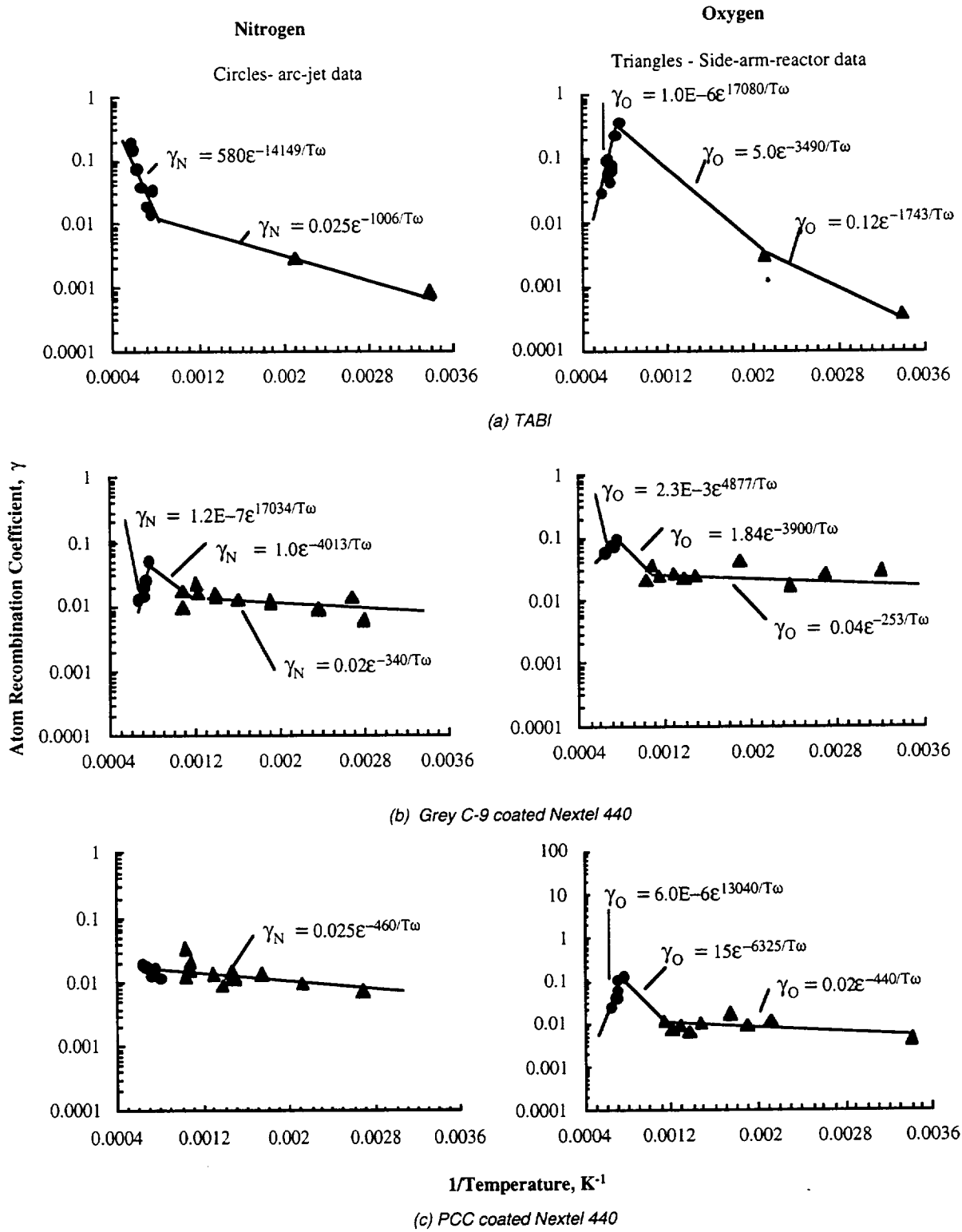


Figure 28. Atom recombination coefficients for blanket TPS.

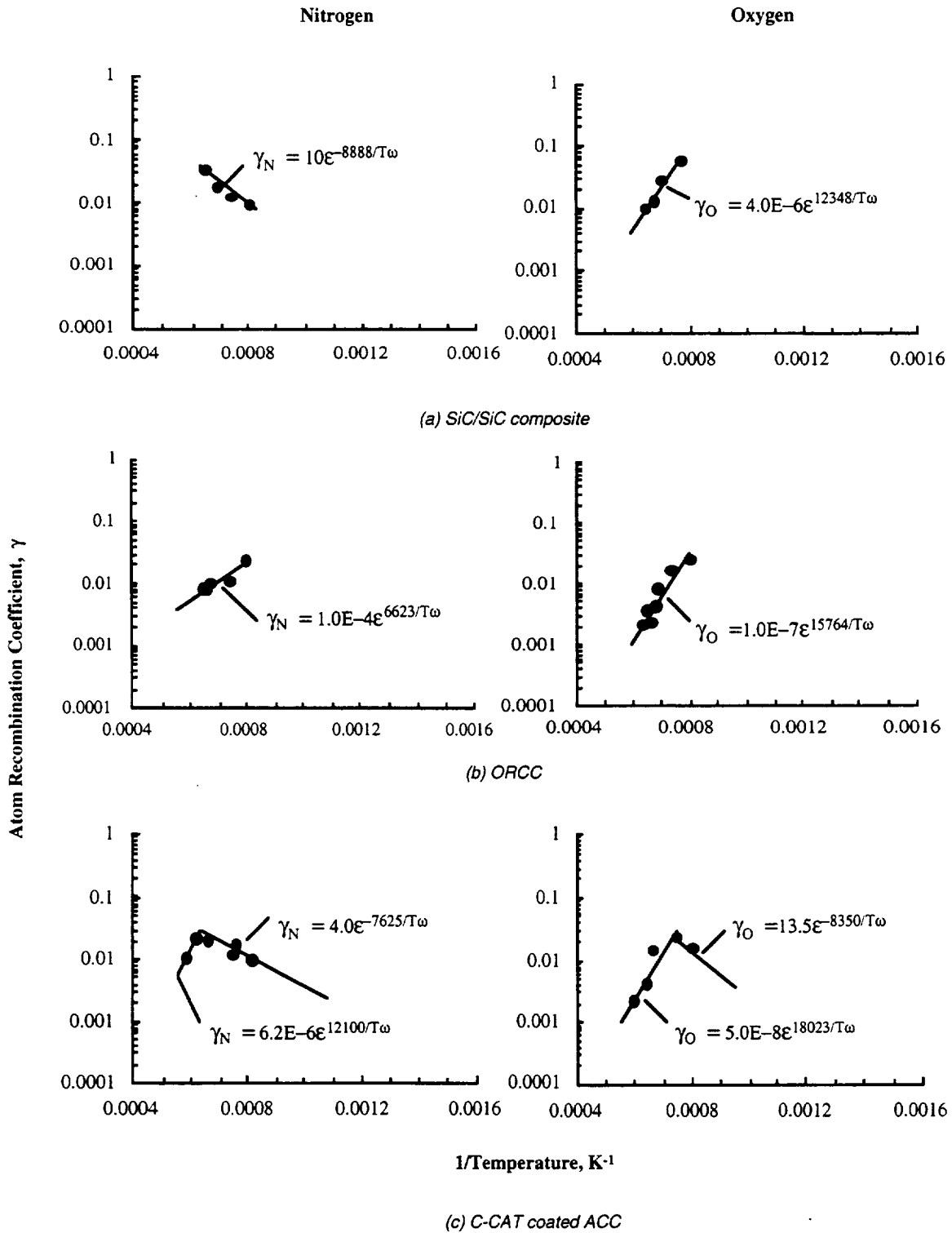


Figure 29. Atom recombination coefficients for advanced carbon composites.

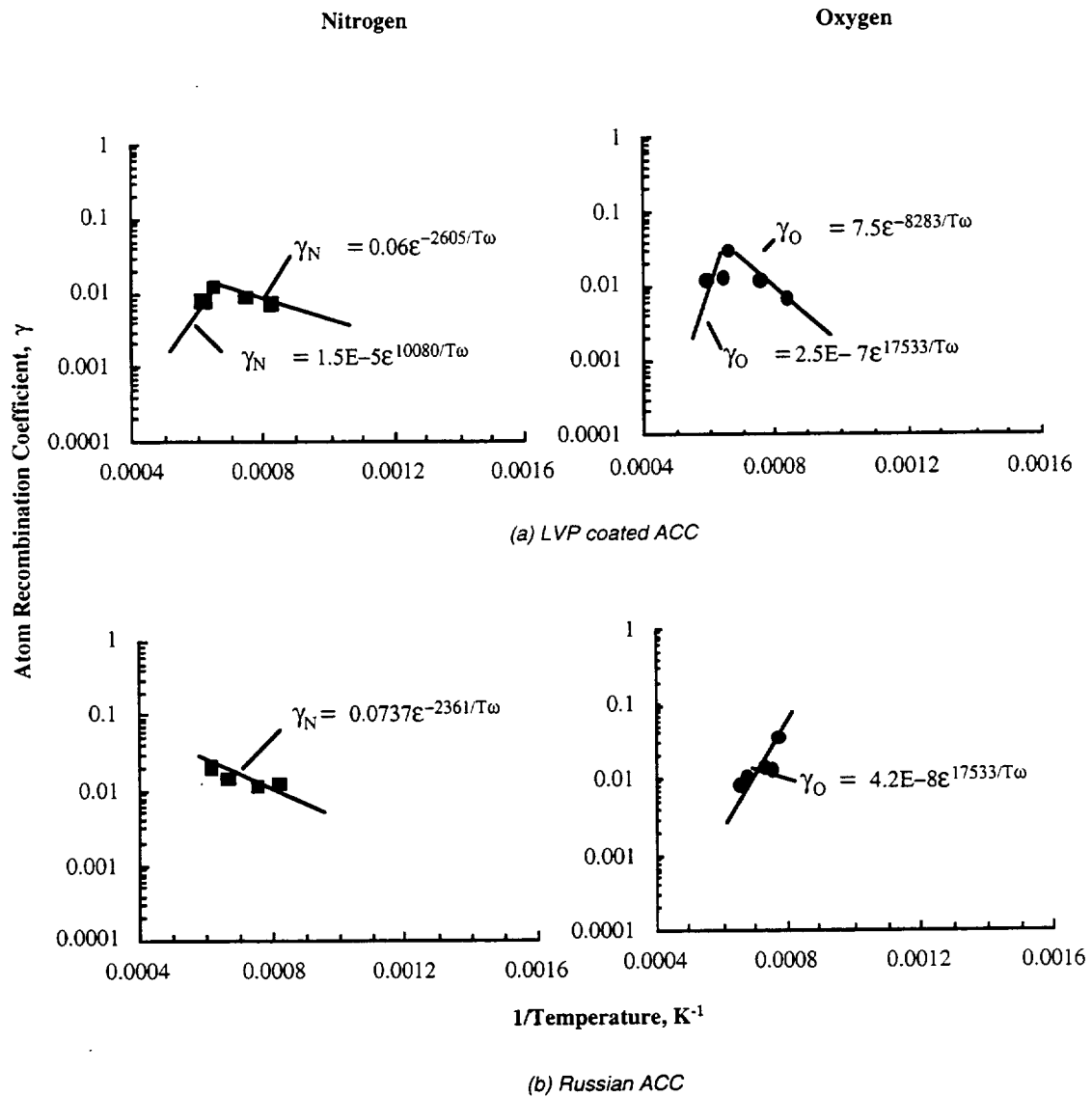


Figure 30. Atom recombination coefficients for advanced carbon composites (concluded).

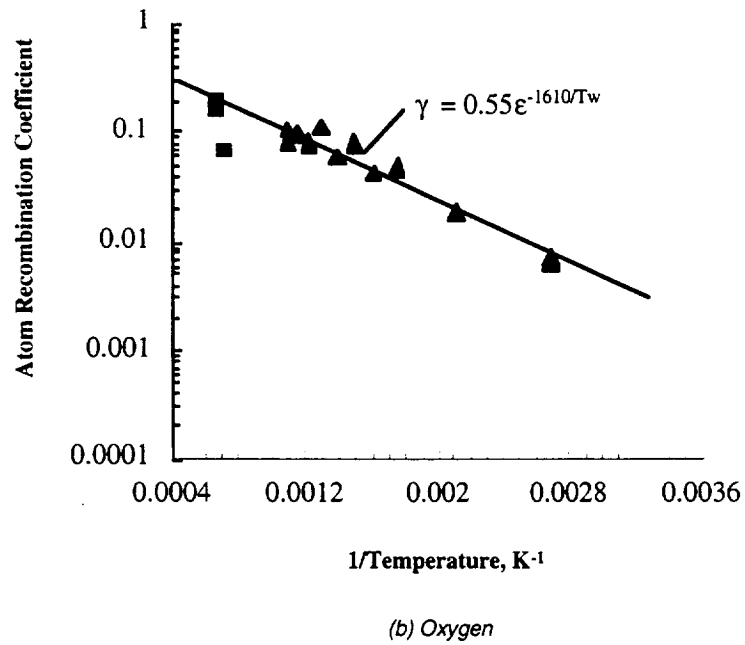
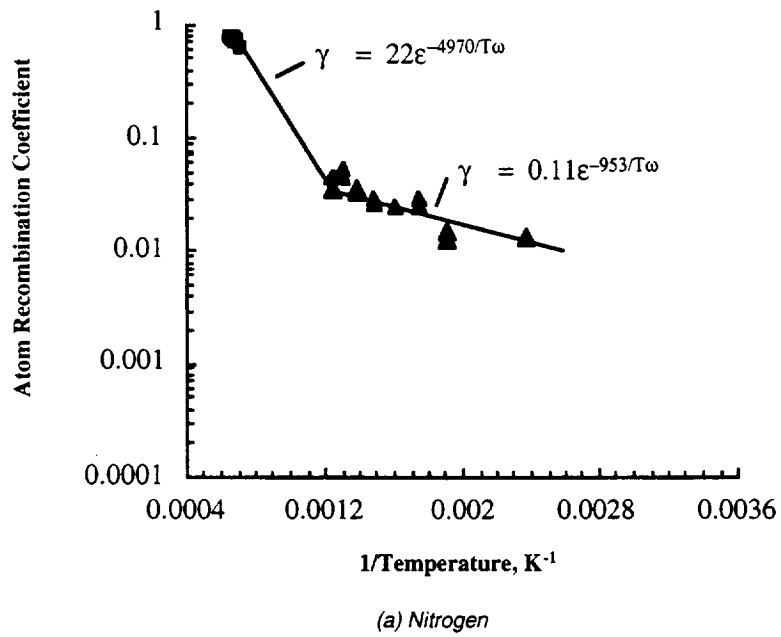


Figure 31. Atom recombination coefficients for Inconel 617.

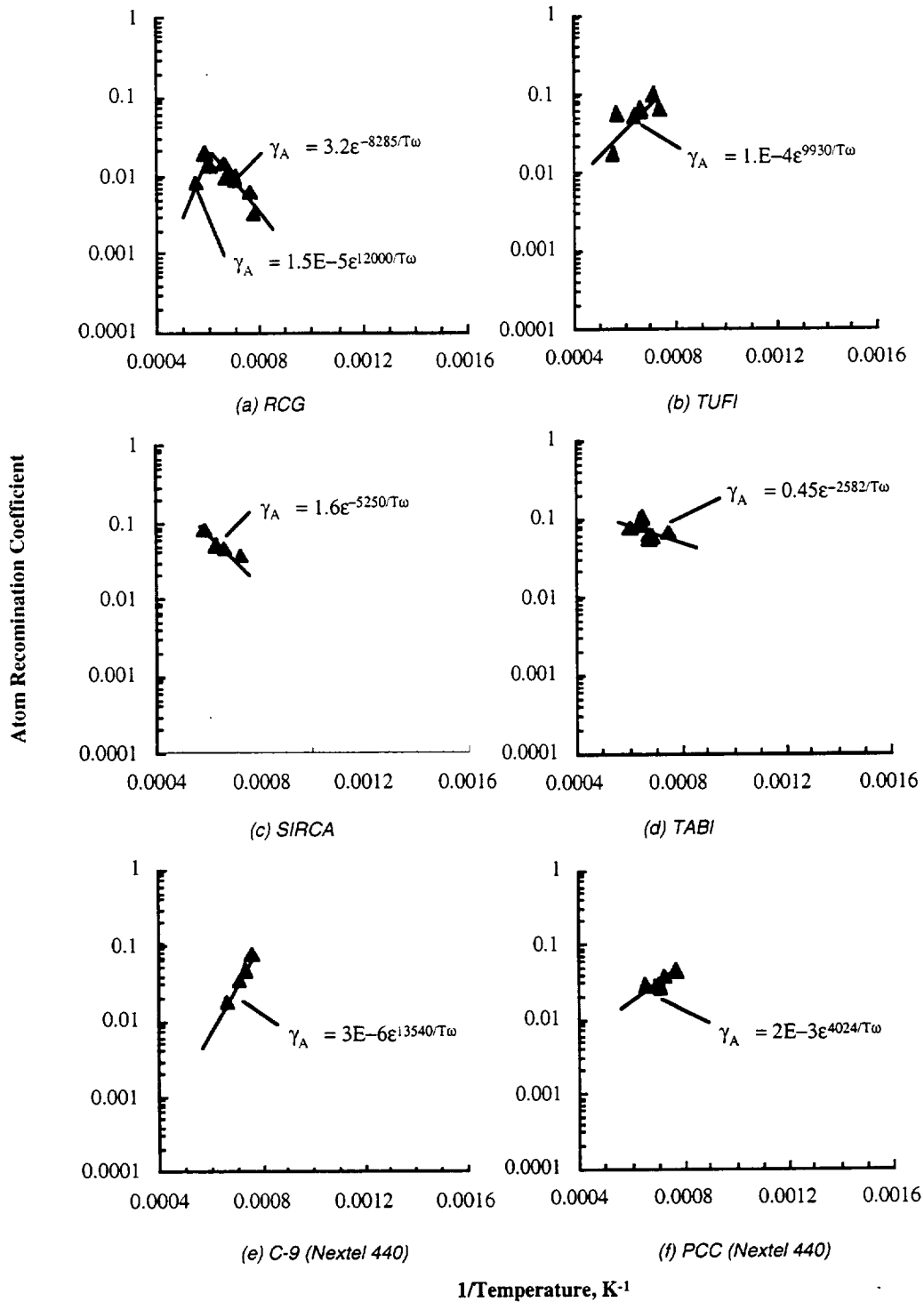


Figure 32. Air recombination coefficients for both rigid and blanket TPS.

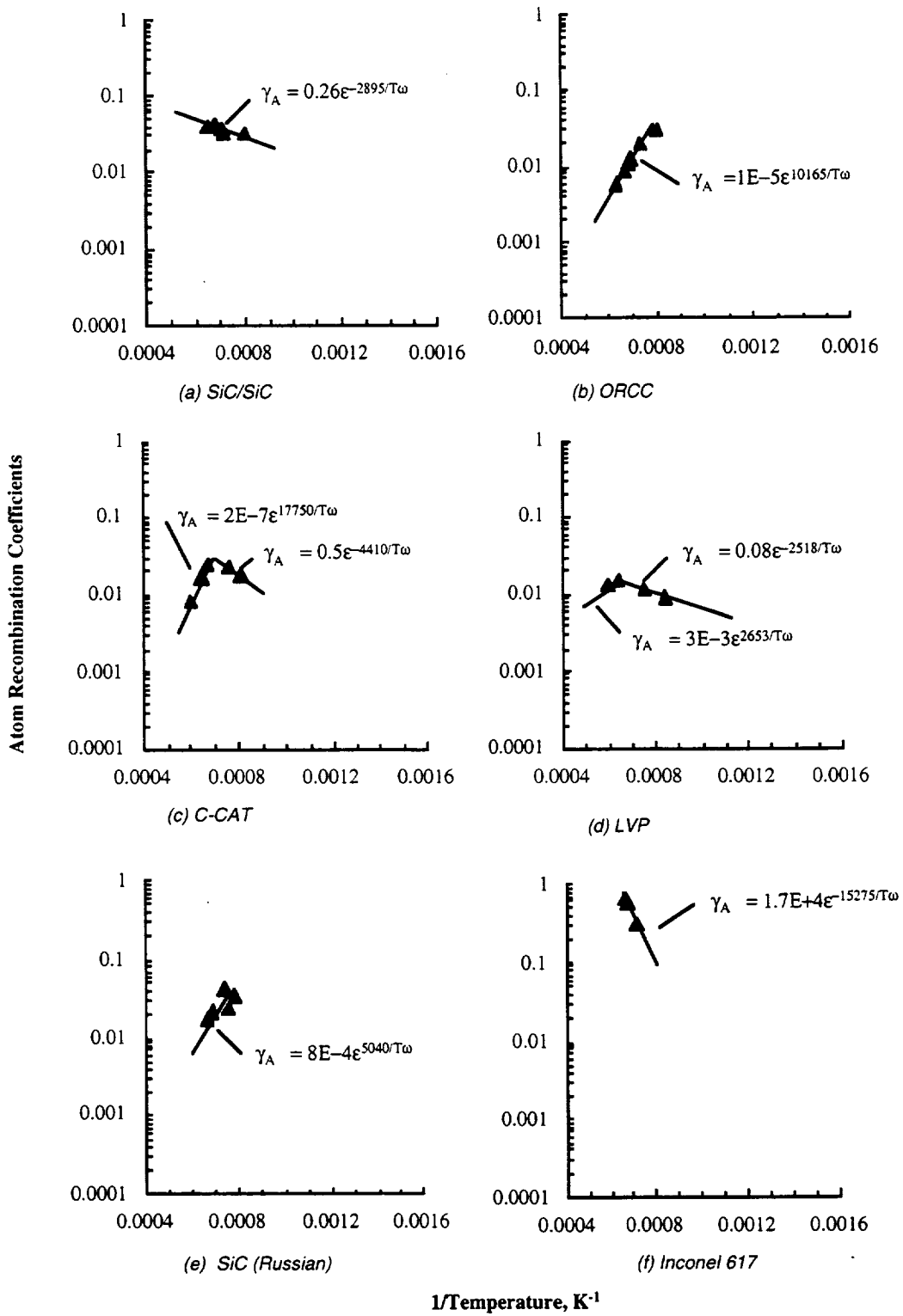
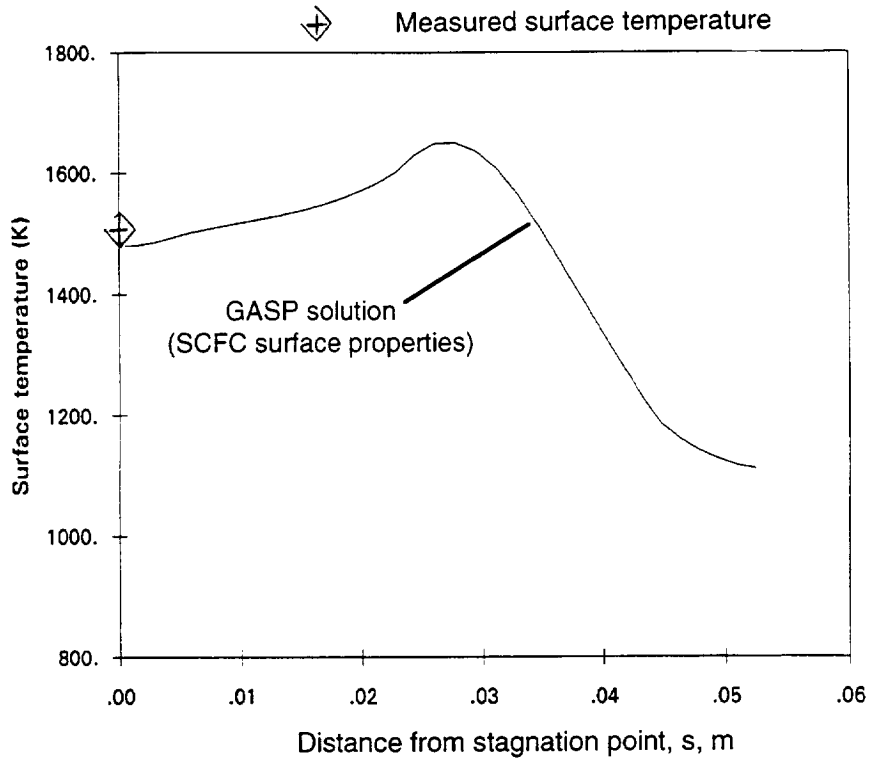
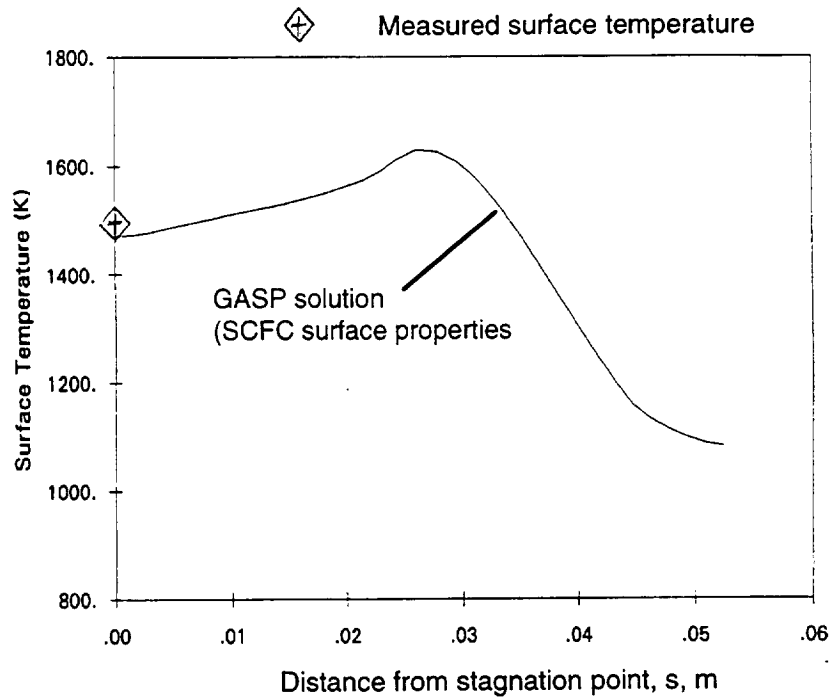


Figure 33. Air recombination coefficients for both carbon composites and metals.



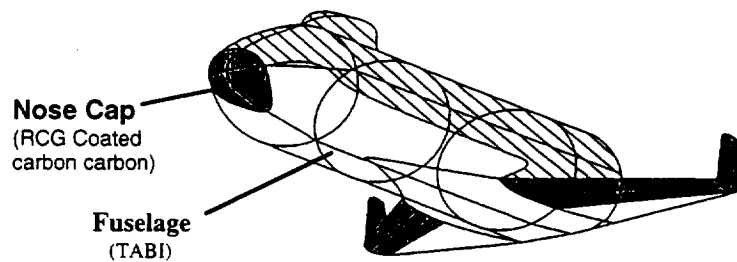
(a) Nitrogen flow



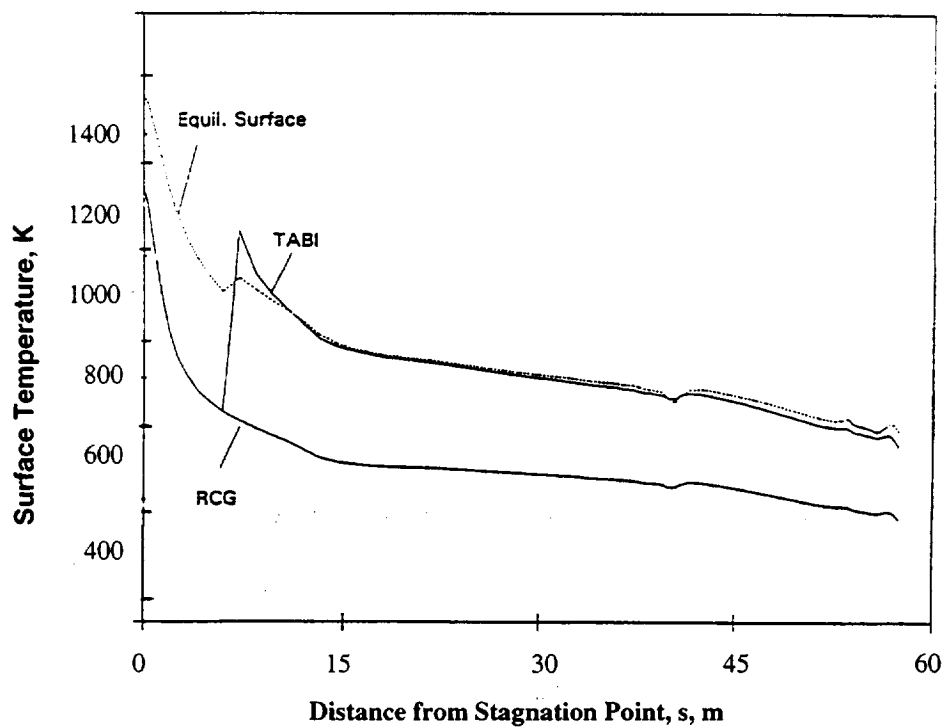
(b) Air flow

Figure 34. Predicted and measured surface temperature on blunt cone during test case 2.

Alt. = 71.5 km  
 $M_\infty = 21.9$   
 $\alpha = 33^\circ$   
 $R_n = 1.55\text{m}$



(a) Typical SSTO



(b) Temperature distribution along SSTO

Figure 35. Effect of surface catalysis on the temperature distribution along an SSTO.



# REPORT DOCUMENTATION PAGE

Form Approved  
OMB No. 0704-0188

Public reporting burden for this collection of information is estimated to average 1 hour per response, including the time for reviewing instructions, searching existing data sources, gathering and maintaining the data needed, and completing and reviewing the collection of information. Send comments regarding this burden estimate or any other aspect of this collection of information, including suggestions for reducing this burden, to Washington Headquarters Services, Directorate for Information Operations and Reports, 1215 Jefferson Davis Highway, Suite 1204, Arlington, VA 22202-4302, and to the Office of Management and Budget, Paperwork Reduction Project (0704-0188), Washington, DC 20503.

<b>1. AGENCY USE ONLY (Leave blank)</b>	<b>2. REPORT DATE</b> July 1997	<b>3. REPORT TYPE AND DATES COVERED</b> Technical Memorandum	
<b>4. TITLE AND SUBTITLE</b> Surface Catalysis and Characterization of Proposed Candidate TPS for Access-to-Space Vehicles		<b>5. FUNDING NUMBERS</b>  242-30-01	
<b>6. AUTHOR(S)</b> David A. Stewart			
<b>7. PERFORMING ORGANIZATION NAME(S) AND ADDRESS(ES)</b> Ames Research Center Moffett Field, CA 94035-1000		<b>8. PERFORMING ORGANIZATION REPORT NUMBER</b>  A-976955	
<b>9. SPONSORING/MONITORING AGENCY NAME(S) AND ADDRESS(ES)</b> National Aeronautics and Space Administration Washington, DC 20546-0001		<b>10. SPONSORING/MONITORING AGENCY REPORT NUMBER</b>  NASA TM-112206	
<b>11. SUPPLEMENTARY NOTES</b> Point of Contact: David A. Stewart, Ames Research Center, MS 234-1, Moffett Field, CA 94035-1000 (415) 604-6614			
<b>12a. DISTRIBUTION/AVAILABILITY STATEMENT</b>  Unclassified — Unlimited Subject Category 16		<b>12b. DISTRIBUTION CODE</b>	
<b>13. ABSTRACT (Maximum 200 words)</b>  Surface properties have been obtained on several classes of thermal protection systems (TPS) using data from both side-arm-reactor and arc-jet facilities. Thermochemical stability, optical properties, and coefficients for atom recombination were determined for candidate TPS proposed for single-stage-to-orbit vehicles. The systems included rigid fibrous insulations, blankets, reinforced carbon carbon, and metals. Test techniques, theories used to define arc-jet and side-arm-reactor flow, and material surface properties are described. Total hemispherical emittance and atom recombination coefficients for each candidate TPS are summarized in the form of polynomial and Arrhenius expressions.			
<b>14. SUBJECT TERMS</b> TPS surface properties, Thermal protection systems, Surface catalysis, Catalytic efficiency, Space vehicle materials		<b>15. NUMBER OF PAGES</b> 59	
		<b>16. PRICE CODE</b> A04	
<b>17. SECURITY CLASSIFICATION OF REPORT</b> Unclassified	<b>18. SECURITY CLASSIFICATION OF THIS PAGE</b> Unclassified	<b>19. SECURITY CLASSIFICATION OF ABSTRACT</b>	<b>20. LIMITATION OF ABSTRACT</b>